

Noble Metal-Free Nanocatalysts with Vacancies for Electrochemical Water Splitting

Min-Quan Yang, Jing Wang, Hao Wu, and Ghim Wei Ho*

The fast development of nanoscience and nanotechnology has significantly advanced the fabrication of nanocatalysts and the in-depth study of the structural-activity characteristics of materials at the atomic level. Vacancies, as typical atomic defects or imperfections that widely exist in solid materials, are demonstrated to effectively modulate the physicochemical, electronic, and catalytic properties of nanomaterials, which is a key concept and hot research topic in nanochemistry and nanocatalysis. The recent experimental and theoretical progresses achieved in the preparation and application of vacancy-rich nanocatalysts for electrochemical water splitting are explored. Engineering of vacancies has shown to open up a new avenue beyond the traditional morphology, size, and composition modifications for the development of nonprecious electrocatalysts toward efficient energy conversion. First, an introduction followed by discussions of different types of vacancies, the approaches to create vacancies, and the advanced techniques widely used to characterize these vacancies are presented. Importantly, the correlations between the vacancies and activities of the vacancy-rich electrocatalysts via tuning the electronic states, active sites, and kinetic energy barriers are reviewed. Finally, perspectives on the existing challenges along with some opportunities for the further development of vacancy-rich noble metal-free electrocatalysts with high performance are discussed.

1. Introduction

The ever-increasing demand of energy as well as the deterioration of global climate and environment has spurred continuous research efforts to explore novel eco-friendly technologies, such as photocatalysis,^[1–13] electrocatalysis,^[2,14–22] supercapacitors,^[14,23–29] and batteries,^[30–37] for the utilization of green and renewable energy resources. Electrochemical water splitting,

which includes the water reduction half-reaction at the cathode (hydrogen evolution reaction, HER) and water oxidation half-reaction at the anode (oxygen evolution reaction, OER) (Figure 1a), is among the most promising energy conversion technologies to address these challenges.^[38–42] The water electrolysis can be regarded as a reverse reaction of H₂ combustion. The combination of the two inverse transformations can form a close cycle that enables the energy conversion and flow with zero carbon footprint.^[43,44] In addition, the electricity that drives the decomposition of water can be derived from solar, wind, hydro, and geothermal energies.^[39,42,45] The sustainable energy conversion not only realizes the storage of these renewable energy resources as chemical fuels through water electrolysis, but also bridges the gaps between continuous applications and the temporal or spatial intermittencies of these energy resources (Figure 1b).

Theoretically, the catalytic decomposition of water into H₂ and O₂ requires a minimum energy input of $\Delta G =$

237.1 kJ mol⁻¹ that corresponds to an applied voltage of 1.23 V to provide the thermodynamic driving force for the uphill reaction.^[46,47] However, in practice, a substantially larger voltage is generally required because of the practical overpotentials associated with the sluggish reaction kinetics, especially for the OER which is a four-electron transfer process.^[39,48,49] The present commercial electrolyzers typically operate at a voltage of 1.8–2.0 V.^[46,49,50] The excess voltage input inevitably impacts on the cost and conversion efficiency. As a result, although the electricity-driven water splitting possesses fascinating perspective of producing clean and sustainable energy, its widespread implementation is still lacking. At present, the contribution of electrochemical water splitting to the global hydrogen fuel production is about 4%.^[41,42]

To realize the envisioning of large-scale water electrolysis for commercialization, improvement in the reaction kinetics and minimization of the overpotential of electrolysis process through the implementation of high-efficiency electrocatalysts is essential.^[41,47] Traditionally, platinum (Pt) metal is the most efficient for HER,^[47,51] and the iridium/ruthenium oxides (IrO₂/RuO₂) are highly active toward the OER.^[50,52,53] Nonetheless, due to the well-known limitations of scarcity, high cost, dissolution, and corrosion during the electrolysis process,^[53–55]

Dr. M.-Q. Yang, Dr. J. Wang, Dr. H. Wu, Prof. G. W. Ho
Department of Electrical and Computer Engineering
National University of Singapore
4 Engineering Drive 3, Singapore 117583, Singapore
E-mail: elehwg@nus.edu.sg

Prof. G. W. Ho
Engineering Science Programme
National University of Singapore
9 Engineering Drive 1, Singapore 117575, Singapore

Prof. G. W. Ho
Institute of Materials Research and Engineering
A*STAR (Agency for Science, Technology and Research)
3 Research Link, Singapore 117602, Singapore

The ORCID identification number(s) for the author(s) of this article can be found under <https://doi.org/10.1002/sml.201703323>.

DOI: 10.1002/sml.201703323

these noble-metal-based catalysts are economically not viable for wide-scale application. Consequently, tremendous endeavors have been devoted to exploring inexpensive, abundant, yet efficient catalytic materials with comparable performance to these noble-metal-based catalysts. Till now, a wide variety of transition-metal (e.g., Mo, Fe, Co, and Ni) oxides, hydroxides, chalcogenides, phosphides, nitrides, carbides, and their inherited composite electrocatalysts have been developed.^[41–44,48–50,56–65] Owing to their low cost, high activity, and stability, these materials are considered to be promising alternatives for the practical water-splitting application. So far, the achievements realized in this area have been summarized by some excellent reviews.^[41–44,48–50,56–61] However, these reports mainly focus on tuning the dimensionalities, designing novel structures, or constructing multicomponent hybrid materials, whereas the importance of vacancies that profoundly influence the functionalities of the nanomaterials is often neglected.

In fact, it has been known that the intrinsic vacancies exist virtually in all solid materials because of the imperfect arrangement of atoms.^[66,67] Particularly, with the significant advancement of nanoscience and nanotechnology, intentional vacancies can now be artificially and controllably introduced into nanocatalyst systems for functional purposes. Over the past decades, the extensive researches in fabricating solid materials with nanoscale size have revealed that the size reduction would remarkably promote the exposure of interior atoms on the surfaces and induce easy escape of atoms from the lattice, which will result in the formation of high-content vacancies.^[68,69] The study of vacancies has become a key concept and hot research topic in the field of solid state nanomaterials. The manipulation of the vacancies effectively modulates the physicochemical, electronic, and thus catalytic properties of nanomaterials, which thereupon inspires the exploration of vacancy-rich nanomaterials for wide applications including solar/fuel cells, supercapacitors, ion batteries, and catalysis.^[66,67,70–72]

Most recently, the experimental and theoretical breakthroughs in electrocatalysis have revealed that the vacancies play important roles in tuning the functionalities of transition-metal-based nanocatalysts, which can (i) act as active sites or promote the exposure of active sites, thus increasing the overall density of catalytic active sites;^[73–78] (ii) form new gap states within the bandgap and/or narrow the bandgap of the electrocatalysts, thereby enhancing the electrical conductivity for fast charge transfer;^[79–83] and (iii) lower the energy barriers and favor the adsorption/desorption of water molecules or intermediate reaction species (e.g., *H for HER; *OH, *OOH for OER) on the surface of the electrocatalyst, hence optimizing the reaction kinetics.^[74,84–88] Taken together, substantial electrocatalytic activity enhancement can be attained by rational design and engineering of the vacancies in nanocatalysts. Moreover, careful in-depth studies of the vacancies in nanocatalysts promote the understanding of structure–catalytic functions at the atomic level. This in turn brings more fundamental insights into the design of advanced catalysts. The achievements realized in the preparation and application of vacancy-rich electrocatalysts have opened up a new avenue for the development of nonprecious metal-based electrocatalysts for efficient energy conversion.



2D materials for applications in photocatalysis and electrocatalysis.

Min-Quan Yang received his Ph.D. degree in Physical Chemistry in 2015 from State Key Laboratory of Photocatalysis on Energy and Environment, Fuzhou University, P. R. China. He is currently a research fellow at the National University of Singapore (NUS). His main research interests

focus on the synthesis of



Jing Wang received his B.Sc. degree in Chemistry Engineering and Technology (2007) and Ph.D. degree in Chemical Engineering (2012) from Nanjing Tech University. He is currently a research fellow at the National University of Singapore (NUS), mainly focusing on the design and synthesis of nanomaterials for photo/electrocatalysis.



Ghim Wei Ho received her Ph.D. in semiconductor nanostructures at the Nanoscience Centre, University of Cambridge in 2006. She is an Associate Professor at the Department of Electrical and Computer Engineering at the National University of Singapore (NUS). She is also one of the pioneer associates of the Engineering Science Programme (ESP) at NUS. Her research thrust is focused on the development of nanostructured materials for photocatalytic and electrocatalytic applications.

Programme (ESP) at NUS. Her research thrust is focused on the development of nanostructured materials for photo-

As such, facing the increasing research efforts and significances of this topic, we herein aim to provide an overview of the recent achievements in both experimental approaches and the theoretical modelings of implementing vacancy-rich nanocatalysts for water electrolysis (Figure 1c). In the following sections, we first discuss the main categories of vacancies in the available nanocatalysts. Then, a summary of the approaches reported to create vacancies in electrocatalysts and the advanced techniques widely used to characterize the vacancies are presented. Moreover, the correlations between the vacancies and electrochemical activities of the vacancy-rich electrocatalysts are elaborately reviewed. Finally, a summary of the research advances and key challenges, along with some perspectives of

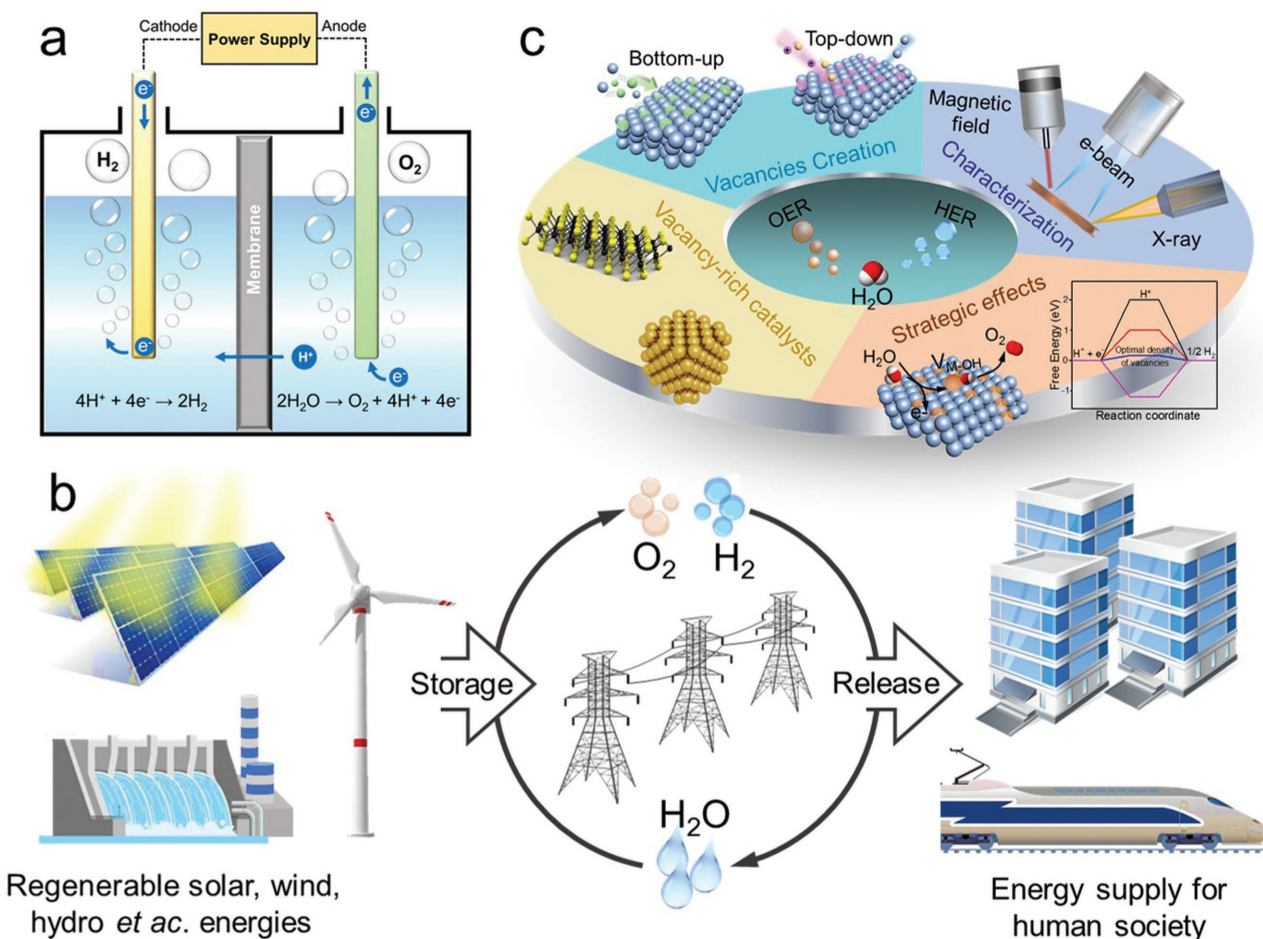


Figure 1. a) Schematic illustration of electrochemical water splitting. b) Energy conversion and utilization cycle of electrochemical water splitting. c) Overview contents of the review.

the future research directions for developing high-performance vacancy-rich electrocatalyst materials, are discussed.

2. Classification of Functional Vacancies

Vacancies are the simplest defects that exist in all of the materials above absolute zero (0 K), which correspond to the absence of atoms at the lattice sites. The presence of vacancies will change the entropy and enthalpy of a material system. Thus, to reach a minimum free energy, there is a thermodynamically stable concentration of vacancies at a given temperature (above 0 K) of a system.^[66] The equilibrium concentration of vacancies C_v , denoted as the ratio of the number of vacancies N_v to the number of atomic sites N , can be estimated by the Boltzmann distribution according to statistical thermodynamics

$$C_v = \frac{N_v}{N} = \exp\left(-\frac{Q_v}{K_B T}\right) \quad (1)$$

where Q_v is the energy required to remove one atom from its lattice site and form a vacant site in a perfect crystal, K_B is

the Boltzmann constant, and T is the absolute temperature. According to the above equation, the thermal equilibrium vacancies will be present in all materials. Moreover, in the case of nonstoichiometric compounds, they may contain vacancies with concentrations far above thermal equilibrium. As a result, a large number of compounds with diverse high concentration of vacancies have been developed.

To date, a host of the reported vacancy-rich transition-metal-based nanocatalysts in both water reduction and oxidation are compounds, which consist of at least two different kinds of atoms with opposite charges (ions), as summarized in **Table 1**. In general, these nanocatalysts are made with deficient metal atoms (cations) or nonmetal atoms (anions), i.e., vacancies at the cation or anion site. Most recently, reports show that cation and anion vacancies coexist in one material system. Therefore, in terms of the deficient component, the vacancies in the reported electrocatalysts are classified into three different types: anion vacancies, cation vacancies, and multi (anion and cation) vacancies (**Figure 2a**). These vacancies have shown to significantly improve the electrochemical water-splitting efficiency, which will be briefly presented in the following section. As for the specific functions of these vacancies toward enhancing the electrocatalytic activity of the

Table 1. Summary of the vacancy-rich nonprecious transition-metal-based electrocatalysts for water splitting. (Note: The “V” represents the materials with vacancies while the “C” denotes the control samples for comparison; N.A. refers to not available).

Material	Vacancy type	Synthetic method	Performance				Ref. [Year]
			Reaction	Electrolyte	Overpotential (η vs RHE) at 10 mA cm ⁻² [mV]	Tafel slope [mV dec ⁻¹]	
Co ₃ O ₄ nanosheets	Oxygen vacancy	Ar-plasma etching	OER	0.1 M KOH	V: 300 C: pristine Co ₃ O ₄ , 540	V: 68 C: 234	[78] [2016]
CoFe LDH nanosheets	O, Co, Fe multiple vacancies	Ar-plasma etching	OER	1 M KOH	V: 266 C: bulk CoFe LDHs, 321	V: 37.85 C: 57.05	[107] [2017]
CoFe LDH nanosheets	O, Co, Fe multiple vacancies	Water plasma etching	OER	1 M KOH	V: 290 C: pristine CoFe LDHs, 332	V: 36 C: 52	[108] [2017]
N-doped Co ₃ O ₄ nanosheets	Oxygen vacancy	N ₂ -plasma etching	OER	0.1 M KOH	V: 310 C: pristine Co ₃ O ₄ , 560	V: 59 C: 234	[94] [2017]
NiCo ₂ O ₄ nanosheets	Oxygen vacancy	Thermal treatment	OER	1 M KOH	V: 326 C: mesoporous Co ₃ O ₄ , 410	V: 30 C: 57	[98] [2015]
La _{0.95} FeO _{3-δ}	Oxygen vacancy	Thermal treatment	OER	0.1 M KOH	V: 410 C: LaFeO _{3-δ} , 510	V: 48 C: 77	[106] [2016]
Porous Co ₃ O ₄	Oxygen vacancy	Calcination of ZIF-67-Co	OER	0.1 M KOH	V: 450 C: ZIF-67, unable to reach 10 mA cm ⁻² at 1.8 V	V: 89 C: 122	[133] [2015]
Single-crystal CoO nanorods	Oxygen vacancy	Thermal treatment	OER	1 M KOH	V: 330 C: polycrystalline CoO, 420	V: 44 C: 62	[85] [2016]
NiCo ₂ O _{4-δ}	Oxygen vacancy	Thermal treatment	OER	0.1 M KOH	V: 390 C: Co ₃ O _{4-δ} , 440 MnCo ₂ O _{4-δ} , 530	V: N.A. C: Co ₃ O _{4-δ} , N.A. MnCo ₂ O _{4-δ} , N.A.	[134] [2015]
5% Ni-Co ₃ O ₄	Oxygen vacancy	Thermal treatment	OER	0.1 M KOH	V: 381 C: undoped mesoporous Co ₃ O ₄ , 390	V: 72.5 C: 74.3	[135] [2016]
Reduced Co ₃ O ₄ nanowires	Oxygen vacancy	NaBH ₄ reduction	OER	1 M KOH	V: 400 C: pristine Co ₃ O ₄ , unable to reach 10 mA cm ⁻² at 1.7 V	V: 72 C: 82	[83] [2014]
Iron-cobalt oxide nanosheets	Oxygen vacancy	NaBH ₄ reduction	OER	0.1 M KOH	V: 308 C: iron-cobalt oxide nanoparticles, 400	V: 36.8 C: 71.7	[92] [2017]
Reduced Co ₃ O ₄ nanoparticles	Oxygen vacancy	NaBH ₄ reduction	OER	1 M KOH	V: 340 C: Co ₃ O ₄ , =390	V: 47 C: 72	[136] [2016]
CaMnO _{2.5} perovskite	Oxygen vacancy	Reduction by annealing in H ₂	OER	0.1 M KOH	V: N.A. C: CaMnO ₃ precursor, N.A.	V: 149 C: 197	[75] [2014]
Layered PrBaMn ₂ O _{5+δ}	Oxygen vacancy	Reduction by annealing in H ₂	OER	0.1 M KOH	V: 500 C: pristine PrBaMn ₂ O _{5+δ} , unable to reach 10 mA cm ⁻² at 1.8 V	V: N.A. C: N.A.	[100] [2016]
Co ₃ O ₄ /rGO composites	Oxygen vacancy	Hydrothermal synthesis	OER	1 M KOH	V: 290 C: 380	V: 68 C: 95	[93] [2017]
Ni-doped CoFe ₂ O ₄ nanospheres	Oxygen vacancy	Hydrothermal synthesis	OER	0.1 M KOH	V: 295 C: CoFe ₂ O ₄ , 355	V: N.A. C: N.A.	[137] [2016]
Bi ₂ WO ₆ Nanoplates	Oxygen vacancy	Hydrothermal synthesis	OER	0.5 M Na ₂ SO ₄ (pH = 6.6)	V: 540 C: Bi ₂ O ₃ nanorods and W ₁₈ O ₄₉ nanowires with oxygen vacancy, unable to reach 10 mA cm ⁻² at 1.8 V	V: N.A. C: N.A.	[81] [2016]

Table 1. Continued.

Material	Vacancy type	Synthetic method	Performance				Ref. [Year]
			Reaction	Electrolyte	Overpotential (η vs RHE) at 10 mA cm ⁻² [mV]	Tafel slope [mV dec ⁻¹]	
Co _{1-x} S/rGO nanosheets	Cobalt vacancy	Hydrothermal synthesis	OER	1 M KOH	V: 310 C: Co _{1-x} S, 440	V: 79 C: 118.32	[87] [2017]
Co ₃ O ₄ nanocrystals/ Ti	Oxygen vacancy	Hydrothermal synthesis	OER	1 M phosphate buffer saline solution (pH = 7)	V: 544 C: Ti+Co ₃ O ₄ , unable to reach 10 mA cm ⁻² at 1.8 V	V: 88 C: 261	[138] [2017]
LiCoO ₂ nanosheets	Oxygen vacancy	Chemical exfoliation and hydrothermal	OER	0.1 M KOH	V: 410 C: bulk LiCoO ₂ , unable to reach 10 mA cm ⁻² at 1.8 V	V: 88 C: 156	[91] [2017]
BaTiO _{3-x} perovskite	Oxygen vacancy	Sol-gel method and reductive thermal treatment	OER	0.1 M NaOH	V: ≈330 mV (at 1 mA cm ⁻²) C: IrO ₂ , ≈350 mV (at 1 mA cm ⁻²)	V: N.A. C: N.A.	[139] [2015]
Ni-doped La _{0.8} Sr _{0.2} Mn _{1-x} Ni _x O ₃ nanoparticles	Oxygen vacancy	Sol-gel method and thermal treatment	OER	0.1 M KOH	V: 540 mV (at 5 mA cm ⁻²) C: undoped La _{0.8} Sr _{0.2} MnO ₃ , 710 mV (at 5 mA cm ⁻²)	V: N.A. C: N.A.	[99] [2016]
Spinel NiCo ₂ O ₄ nanowire arrays	Oxygen vacancy	Room-temperature solution reaction	OER	1 M KOH	V: 428 C: NiO, 648 Co ₃ O ₄ , 478	V: 62 C: NiO, 107 Co ₃ O ₄ , 67	[96] [2015]
Reduced NiCo ₂ O ₄ nanosheets	Oxygen vacancy	NaBH ₄ reduction	OER	0.1 M KOH	V: 379 C: RuO ₂ , 376	V: 63.4 C: 76.1	[97] [2016]
Nanoporous CoO _x particles	Oxygen vacancy	Electrochemical etching of CoSn(OH) ₆	OER	1 M KOH	V: 313 C: IrO ₂ , 326	V: N.A. C: IrO ₂ , N.A.	[140] [2016]
Mn ₃ O ₄ @Mn _x Co _{3-x} O ₄ nanoparticles	Oxygen vacancy	Exchange of Co ions with Mn ₃ O ₄	OER	1 M KOH	V: 246 C: RuO ₂ , N.A.	V: 46 C: RuO ₂ , N.A.	[95] [2017]
δ-MnO ₂ nanosheet	Oxygen vacancy	Hydrothermal	OER HER	1 M KOH	V: 320 C: IrO ₂ , 340 V: 196 C: Ni foam, 378	V: 40 C: IrO ₂ , 68 V: 66 C: 89	[79] [2017]
TiO _{1.23} film/Ti foil	Oxygen vacancy	Cathodic reduction	HER	0.5 M H ₂ SO ₄	V: 198 C: TiO ₂ , 700	V: 88 C: 393	[82] [2016]
N-doped CoS ₂	Sulfur vacancy	Thermal treatment	HER	0.5 M H ₂ SO ₄	V: 57 C: CoS ₂ , ≈210	V: 48 C: N.A.	[129] [2017]
Mesoporous MoO _{3-x}	Oxygen vacancy	Thermal treatment	HER	0.1 M KOH 0.1 M H ₂ SO ₄	V: 138 C: commercial MoO ₃ , 314 V: 179 C: commercial MoO ₃ , 422	V: 56 C: 130 V: 72 C: 146	[141] [2016]
WSe ₂ monolayer nanosheets	Selenium vacancy	Reduction by annealing in H ₂	HER	0.5 M H ₂ SO ₄ 1 M KOH	V: 245 C: WSe ₂ , 563 V: 316 C: WSe ₂ , ≈760	V: 76 C: 95 V: 103 C: 265	[76] [2016]
Ta-doped WO ₃	Oxygen vacancy	Hydrothermal synthesis	HER	1 M H ₂ SO ₄	V: ≈520 C: WO ₃ , unable to reach 10 mA cm ⁻² at -0.52 V	V: 65 C: 90	[142] [2014]
Mesoporous 1T phase MoS ₂ nanosheets	Sulfur vacancy	Liquid-ammonia-assisted lithiation	HER	0.5 M H ₂ SO ₄	V: 153 C: 1T MoS ₂ nanosheets, 203	V: 43 C: 48	[101] [2016]

Table 1. Continued.

Material	Vacancy type	Synthetic method	Performance				Ref. [Year]
			Reaction	Electrolyte	Overpotential (η vs RHE) at 10 mA cm ⁻² [mV]	Tafel slope [mV dec ⁻¹]	
WO ₂ -carbon	Oxygen vacancy	Calcination of WO ₃ -ethylenediamine	HER	0.5 M H ₂ SO ₄	V: 58	V: 48	[113] [2015]
					C: WO ₃ porous nanowires, 203	C: 56	
P-doped MoO _{3-x} nanosheets	Oxygen vacancy	Thermal treatment in N ₂	HER	0.5 M H ₂ SO ₄	V: 166 C: MoO ₃ /4-BBPA, 407	V: 42 C: 98	[143] [2017]
MoS ₂	Sulfur vacancy	Liquid exfoliation by NH ₃	HER	0.5 M H ₂ SO ₄	V: 160 C: MoS ₂ -NH ₃ , 230	V: 54.9 C: 55.3	[103] [2016]
MoS ₂ monolayer	Sulfur vacancy	Remote H ₂ -plasma etching	HER	0.5 M H ₂ SO ₄	V: 183 C: pristine MoS ₂ , 727	V: 77.6 C: 164.5	[104] [2016]
MoS ₂	Sulfur vacancy	Electrochemical desulfurization	HER	0.5 M H ₂ SO ₄	V: ≈320 C: pristine MoS ₂ , N.A.	V: 102 C: 151	[73] [2017]
	Sulfur vacancy	Ar-plasma etching	HER	0.5 M H ₂ SO ₄ (pH = 0.2)	V: 170 C: pristine MoS ₂ , N.A.	V: 60 C: 98	[74] [2016]
Monolayer 2H-MoS ₂							
Amorphous MoS _x	Sulfur vacancy	Remote H ₂ -plasma etching	HER	0.5 M H ₂ SO ₄	V: 143 C: pristine MoS _x , 206	V: 39.5 C: 84.2	[84] [2016]
MoSe _{2-x} nanosheets	Selenium vacancy	Bottom-up colloidal synthesis	HER	0.5 M H ₂ SO ₄	V: 288 C: bulk MoSe ₂ , N.A.	V: 98 C: 346	[77] [2014]
3D MoS _{2(1-x)} Se _{2x} nanosheets	Sulfur and selenium vacancies	Ar/H ₂ -assisted CVD growth	HER	0.5 M H ₂ SO ₄	V: 183 C: WS ₂ , 244; WSe ₂ , 220	V: 55.5 C: WS ₂ , 104.2; WSe ₂ , 81.2	[102] [2016]
Defective TiO ₂ /Co@N-doped carbon nanotube (CNT)	Oxygen vacancy	Thermal treatment	HER	0.5 M H ₂ SO ₄	V: 167	V: 73.5	[144] [2017]
					C: Co@N-doped CNT, 260	C: Co@N-doped CNT, 105.1	

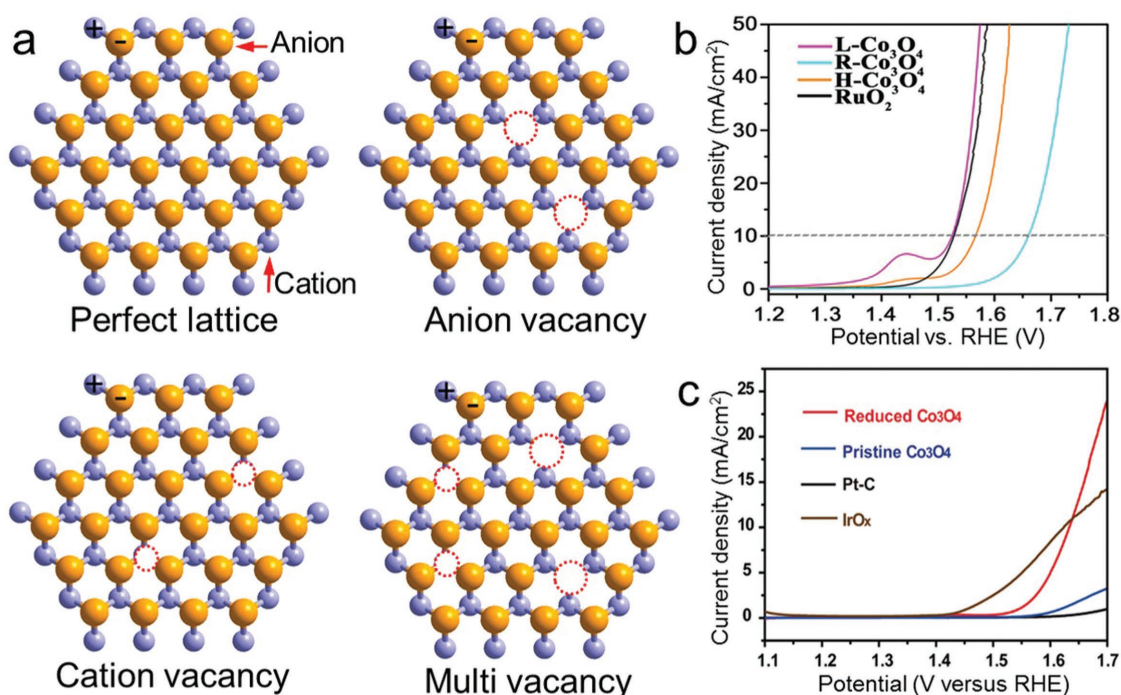


Figure 2. a) The types of vacancies in transition-metal-based electrocatalysts. b) Linear sweep voltammetry (LSV) curves of OER for vacancy-rich Co₃O₄ (L-Co₃O₄), pristine Co₃O₄ (R-Co₃O₄), hydrothermal synthesized Co₃O₄ (H-Co₃O₄) and RuO₂ in 1 M KOH. Reproduced with permission.^[89] Copyright 2016, American Chemical Society. c) LSV curves of OER for vacancy-rich Co₃O₄ (reduced Co₃O₄), pristine Co₃O₄, IrO_x and Pt/C in 1 M KOH. Reproduced with permission.^[83] Copyright 2014, John Wiley & Sons, Inc.

transition-metal-based nonprecious nanocatalysts, the detailed discussion will be presented in Section 5.

2.1. Anion Vacancies

Oxygen vacancy is thus far the most popular anion vacancy in the reported vacancy-rich transition-metal-based electrocatalysts. Owing to the reducibility of M–O (metal–oxygen) bonds and low hopping barriers for oxygen vacancy, the preparation of oxygen-deficient nanomaterials has been extensively reported to enhance the electrocatalysis performance.^[79,89–92,133,144] For instance, Co_3O_4 , which is a typical spinel-type oxide with mixed oxidation states of Co^{2+} located at the tetrahedral site and Co^{3+} occupied the octahedral site, has been demonstrated for facile formation of oxygen-deficient structure by several groups.^[78,83,89,90,93,94] Du and co-workers have prepared Co_3O_4 nanoparticles with abundant oxygen vacancies (L- Co_3O_4) for OER (Figure 2b).^[89] The generation of oxygen vacancies significantly facilitates the adsorption of H_2O molecules, improves the conductivity, and increases the exposure of surface active sites. As a result, the Co_3O_4 displays high catalytic performance with an overpotential of 294 mV (vs reversible hydrogen electrode (RHE)) at 10 mA cm^{-2} and a Tafel slope of 74 mV dec^{-1} , which even outperforms the noble-metal catalyst of RuO_2 (298 mV at 10 mA cm^{-2} and a Tafel slope of 78 mV dec^{-1}). Zheng and co-workers have reported a reduced mesoporous oxygen-deficient Co_3O_4 nanowires for electrochemical O_2 production.^[83] The existence of oxygen vacancies leads to the formation of new gap states

and enhancement of the electrical conductivity. The reduced Co_3O_4 nanowires exhibit a much larger current of 13.1 mA cm^{-2} at 1.65 V versus RHE and a much lower onset potential of 1.52 V than pristine Co_3O_4 nanowires (1.8 mA cm^{-2} at 1.65 V, and an onset potential of 1.57 V) (Figure 2c).

In addition to Co_3O_4 , the oxygen-vacancy-induced electrocatalytic activity enhancement has also been observed in other transition-metal oxides. Recently, Gong and co-workers have devised an edge-site-enriched core-shell $\text{Mn}_3\text{O}_4@\text{Co}_x\text{Mn}_{3-x}\text{O}_4$ oxides nanoparticles (Mn@CoMnO NPs) (inset in Figure 3a) through an ion exchange of Co ions with Mn ions on the surface of Mn_3O_4 seed for OER.^[95] They reveal that the existence of abundant edge sites has promoted the generation of oxygen vacancies in the hybrid particles, which results in the direct structural exposure of Co atoms with open coordination sites, as illustrated in Figure 3b. Such unsaturated coordination sites with missing oxygen atoms are proposed to be unstable in alkaline condition and are easily filled by OH^- groups, which can reduce the overpotential for the H_2O dissociation or favor the OH^- conversion to a more active oxyhydroxide species. Meanwhile, the heterojunction between the cores and shells has contributed to lowering the charge transfer resistance and promoting the charge transport kinetics. As a result, the optimal edge-site-enriched Mn@CoMnO NPs with unsaturated coordination present an overpotential as low as 246 mV at 10 mA cm^{-2} , which is 10 and 46 mV lower than the samples with less edge-site-enriched shells of Mn@CoMnO-90 NPs and Mn@CoMnO-150 NPs, respectively (Figure 3a). Importantly, the performance of the as-prepared Mn@CoMnO NPs even outperforms the commercial benchmark electrocatalyst, RuO_2 .

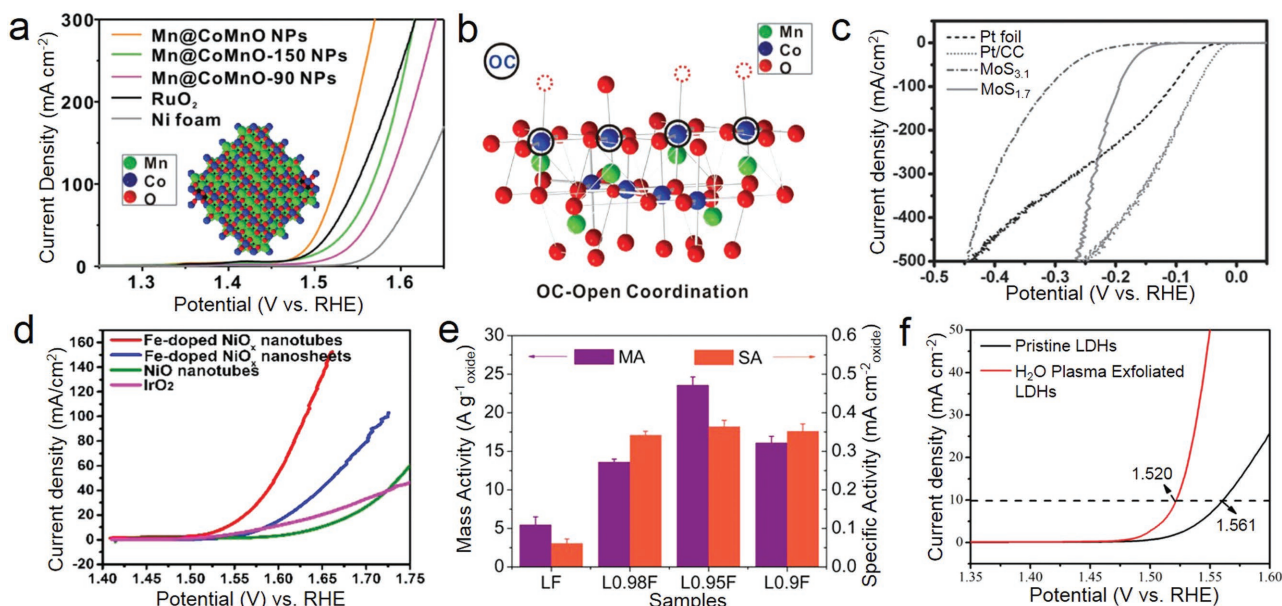


Figure 3. a) LSV curves of OER for Mn@CoMnO NPs, RuO_2 , and Ni foam in 1 M KOH (inset shows the structural model); b) structural illustration of the edge-site-enriched Mn@CoMnO NPs with unsaturated coordination. Reproduced with permission.^[95] Copyright 2017, John Wiley & Sons, Inc. c) LSV curves of HER for Pt foil, Pt/carbon cloth (Pt/CC), $\text{MoS}_{3.1}$, and $\text{MoS}_{1.7}$ in 0.5 M H_2SO_4 . Reproduced with permission.^[84] Copyright 2016, John Wiley & Sons, Inc. d) LSV curves of OER for hierarchical vacancy-rich Fe-doped NiO_x nanotubes, Fe-doped NiO_x nanosheets, NiO nanotubes, and IrO_2 in 1 M KOH. Reproduced with permission.^[105] Copyright 2017, Elsevier. e) OER mass activity (MA) and specific activity (SA) of LaFeO_3 (LF), $\text{La}_{0.98}\text{FeO}_{3-\delta}$ (L0.98F), $\text{La}_{0.95}\text{FeO}_{3-\delta}$ (L0.95F), and $\text{La}_{0.9}\text{FeO}_{3-\delta}$ (L0.9F) catalysts at 1.63 V in 0.1 M KOH. Reproduced with permission.^[106] Copyright 2016, American Chemical Society. f) LSV curves of OER for pristine CoFe LDHs and water-plasma exfoliated CoFe LDH nanosheets with multivacancies. Reproduced with permission.^[108] Copyright 2017, John Wiley & Sons, Inc.

Moreover, CoO ,^[85] MnO_2 ,^[79] NiCo_2O_4 ,^[96–98] and perovskite oxides^[75,80,86,99,100] with abundant oxygen vacancies have also been reported for remarkably improving the electrocatalytic water-splitting efficiencies. These reports together validate the effectiveness of oxygen vacancies in modulating the functionalities of transition-metal-based electrocatalysts and constitute the main body of vacancy-mediated electrocatalysis.

Apart from the oxygen vacancy, sulfur and selenium vacancies are another two commonly reported anion vacancies, which are frequently observed in the metal chalcogenides electrocatalysts such as MoX_2 and WX_2 ($X = \text{S}$ and Se).^[73,74,76,77,84,101–104] The sulfur and selenium vacancies can facilitate favorable hydrogen adsorption and introduce more basal plane active sites. Li and co-workers have developed a high-sulfur-vacancy amorphous MoS_2 (a- $\text{MoS}_{1.7}$) for HER.^[84] The creation of sulfur vacancies leads to a significant enhancement in the performance of a- $\text{MoS}_{1.7}$ (overpotential of 143 mV vs RHE at 10 mA cm^{-2}) compared to its pristine $\text{MoS}_{3.1}$ counterpart (overpotential of 206 mV vs RHE at 10 mA cm^{-2}). In particular, the vacancies also change the surface energy of the catalysts, which inhibits the bubble trapping on catalyst surfaces at high current densities. As a result, the HER performance of the a- $\text{MoS}_{1.7}$ outperforms Pt catalyst at high current density (Figure 3c). Analogously, Cai and co-workers have reported a controllable engineering of selenium vacancies in basal planes of mechanically exfoliated WSe_2 monolayer nanosheets for efficient electrocatalytic H_2 evolution.^[76] The selenium vacancies have been verified to act as highly active and tunable catalytic sites for HER. Consequently, the Se-vacancy-rich WSe_2 exhibits a ≈ 15 times larger current density than WSe_2 nanosheets at the voltage of 400 mV.

2.2. Cation Vacancies

In spite of the fact that anion vacancies are the most common surface defects, recently, some reports have shown that metal cation vacancies can also be prevalent for nanocatalysts.^[87,88,105] The cation vacancies have demonstrated to display similar roles as that of anion vacancies for altering the catalytic properties of nanomaterials. For example, Li and co-workers have prepared a hierarchical Fe-doped NiO_x nanotubes assembled from ultrathin nanosheets.^[105] Investigations suggest that the incorporation of Fe results in abundant trivalent nickel (Ni^{3+}) and nickel vacancies, which drastically modify the local atomic and electronic structure. The as-prepared hierarchical Fe-doped NiO_x nanotubes exhibit outstanding OER activity and stability. As shown in Figure 3d, the overpotential of the vacancy-rich Fe-doped NiO_x nanotubes for achieving a current density of 10 mA cm^{-2} is 310 mV, which is lower than that of Fe-doped NiO_x nanosheets (355 mV), NiO nanotubes (418 mV), and even better than IrO_2 (360 mV). The Tafel slope of hierarchical Fe-doped NiO_x nanotubes is also the smallest (≈ 49 mV dec^{-1}) among the tested catalysts, which reveals the favorable kinetics toward electrochemical OER.

In addition, Xie and co-workers have prepared a cobalt vacancy-rich ultrathin CoSe_2 nanosheets with atomic thickness.^[88] The developed Co-deficient CoSe_2 ultrathin nanosheets effectively catalyze the OER with low overpotential, small Tafel slopes, and large turnover frequencies, which are all superior to those of its bulk counterparts and most reported Co-based

electrocatalysts. Notably, compared to the plentiful studies in construction and exploration of anion vacancy-rich electrocatalysts, the reports of electrocatalysts with abundance metal cation vacancies are limited, which may be hindered by the high formation energy requirement of metal cation vacancies. In this sense, more efforts are needed in this preliminary research area to foster the development of cation vacancy-rich electrocatalysts.

2.3. Multi (Anion and Cation) Vacancies

In addition to the commonly recognized single-type vacancy-rich (anion-rich or cation-rich) nanocatalysts, several recent studies have proven that these two types of vacancies also coexist within one material system and function in a synergistic way to accelerate the water electrolysis process.^[106–108] For example, perovskite oxide is an important class of mixed oxide that offers great flexibility in controlling and tailoring of multi (anion and cation) vacancies. The general formula of perovskite materials is ABO_3 , in which A is a rare-earth or alkaline earth metal element and B is a transition metal element. The numerous combination of mixed A and B cations and nonstoichiometry oxygen may be constructed for enhanced electrocatalysis. Zhou and co-workers have developed an efficient LaFeO_3 perovskite nanocatalyst by tuning cation deficiency for enhancing the electrocatalytic O_2 evolution and reduction activity.^[106] In their work, A-site cation deficiency is introduced merely by changing the amount of La precursor. The La deficiency induces the creation of surface oxygen vacancies and the small amount of Fe^{4+} species in the A-site cation-deficient $\text{La}_{1-x}\text{FeO}_{3-\delta}$, which synergistically promote the $\text{La}_{1-x}\text{FeO}_{3-\delta}$ to display higher OER activity than the pristine LaFeO_3 , as shown in Figure 3e.

Moreover, layered double hydroxides (LDHs) containing multivacancies with enhanced electrocatalytic performance have also been reported recently.^[107,108] LDHs are a class of lamellar ionic crystals consisting of positively charged brucite-like host layers and exchangeable charge-compensating interlayer anions.^[58,108] By etching the charge-balancing anions, hence interrupting the electrostatic interactions, and separating the positively charged host layers from each other, multiple vacancies can be generated. Wang and co-workers have exfoliated bulk CoFe LDHs into ultrathin LDH nanosheets, which contain multivacancies including O, Co, and Fe vacancies.^[108] Owing to their ultrathin 2D structure, the LDH nanosheets expose a greater number of active sites, and the multiple vacancies significantly improve the intrinsic activity for OER (Figure 3f). The as-exfoliated ultrathin CoFe LDH nanosheets exhibit an obvious lower overpotential (290 mV at 10 mA cm^{-2}) and faster kinetics (Tafel slope of 36 mV dec^{-1}) than bulk CoFe LDHs (332 mV at 10 mA cm^{-2} , 52 mV dec^{-1}).

3. Engineering of Functional Vacancies

In light of the success of improving the water-splitting efficiency by vacancies engineering, a number of strategies have been developed to create functional vacancies in transition-metal-based nanomaterials with diverse morphologies. Some of the processes are carried out in conjunc-

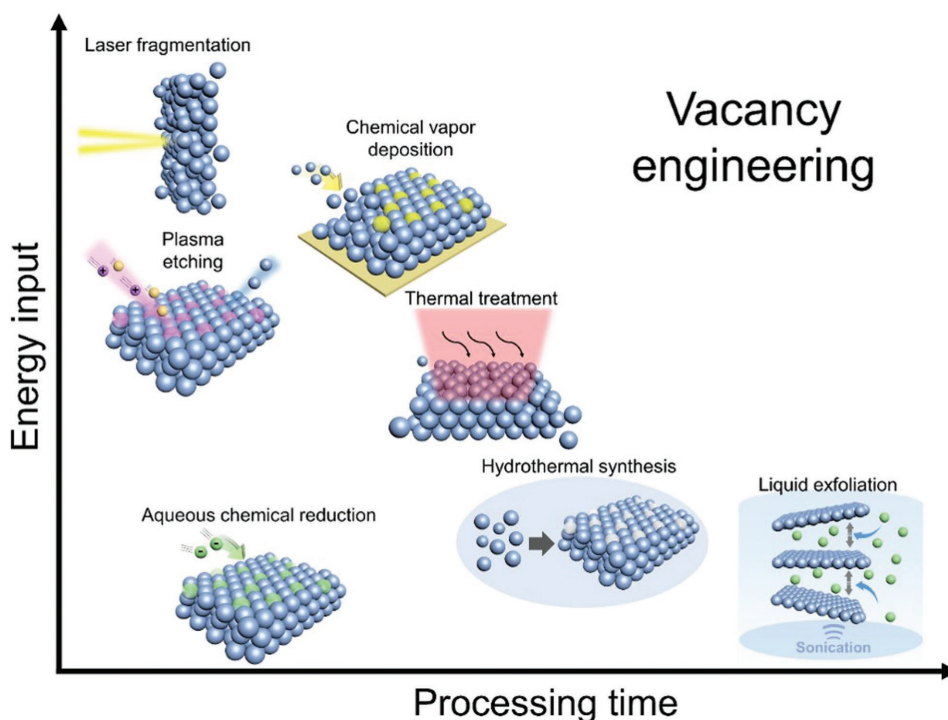


Figure 4. Summary and schematic presentation of the methods reported for the creation of vacancies in transition-metal-based electrocatalysts.

tion with the synthesis, while the other via post-treatment. Broadly, these approaches can be categorized into “top-down” methods, such as liquid exfoliation, plasma etching, or thermal treatment, as well as the “bottom-up” assembly, for instance, hydrothermal and chemical vapor deposition (CVD). In terms of the energy input and processing time, these methods have been summarized and presented schematically in **Figure 4**. Importantly, the density and distribution of the vacancies can be manipulated to a certain extent by controlling the processing parameters, which allows the tuning of the electrocatalytic activity to maximize the efficiency.

3.1. Liquid Exfoliation

Liquid exfoliation refers to the delamination of laminar-structured bulk crystals in liquid dispersions into individual, atomically thin nanosheets with highly exposed surfaces of large planar dimensions.^[109] In order to overcome the binding forces (e.g., van der Waals interactions) between the interlayers, intense means are often used, such as ultrasonication that imposes high-amplitude sonication waves to facilitate the exfoliation. It is reported that some of the atoms on the surface of the electrocatalyst that can be strongly bonded to specific surfactants/intercalators are simultaneously dislodged or displaced from the lattice during the exfoliation, hence producing vacancies. Xie and co-workers have successfully created a large number of cobalt vacancies on the surfaces of ultrathin CoSe_2 nanosheets (**Figure 5a**) by ultrasonic exfoliation of the lamellar hybrid intermediates CoSe_2 -diethylenetriamine (DETA).^[88] The Co atoms that are initially coordinated with DETA are detached from the CoSe_2 lattices under the ultrasonic treatment, leaving

behind vacancies. The as-formed cobalt vacancies can serve as favorable adsorption sites for H_2O molecules to markedly lower the OER overpotential.

Similarly, Xu et al. have also used ultrasonication to exfoliate the ammonia (NH_3)-intercalated MoS_2 into monolayer nanosheets (**Figure 5b**) that are rich in sulfur vacancies.^[103] The NH_3 molecules are adhered to the S–Mo–S layers by van der Waals forces and hydrogen bonds, which can extract the sulfur atoms from the lattices to form sulfur vacancies by the shear sonication and cavitation forces.^[103] The liquid exfoliation technique exhibits simplicity and versatility in obtaining vacancy-rich nanosheets. However, it usually involves lengthy intercalation (hours or even days) and post-treatment steps. This method also relies heavily on the choice of liquid media for good dispersion of bulk materials and the stabilization of as-exfoliated thin nanosheets as poor solvents may cause re-stacking of the nanosheets. Furthermore, the solvent molecules could be adsorbed on the final products, which may block the active sites to reduce the electrocatalytic activity.

3.2. Chemical Reduction

Chemical reduction involves the reaction of electrons (e^-) with atoms in the lattices to form corresponding vacancies in the matrix.^[110] In general, two routes have been reported: (i) the high-temperature annealing in reductive atmosphere, such as hydrogen gas, and (ii) the aqueous chemical reaction using reducing agents. For the first route, the hydrogen that is adsorbed on the nanocatalyst can transfer electrons to the lattice atoms at high temperature, which could reduce the catalysts and lead to the formation of vacancies. Sun et al. have introduced selenium

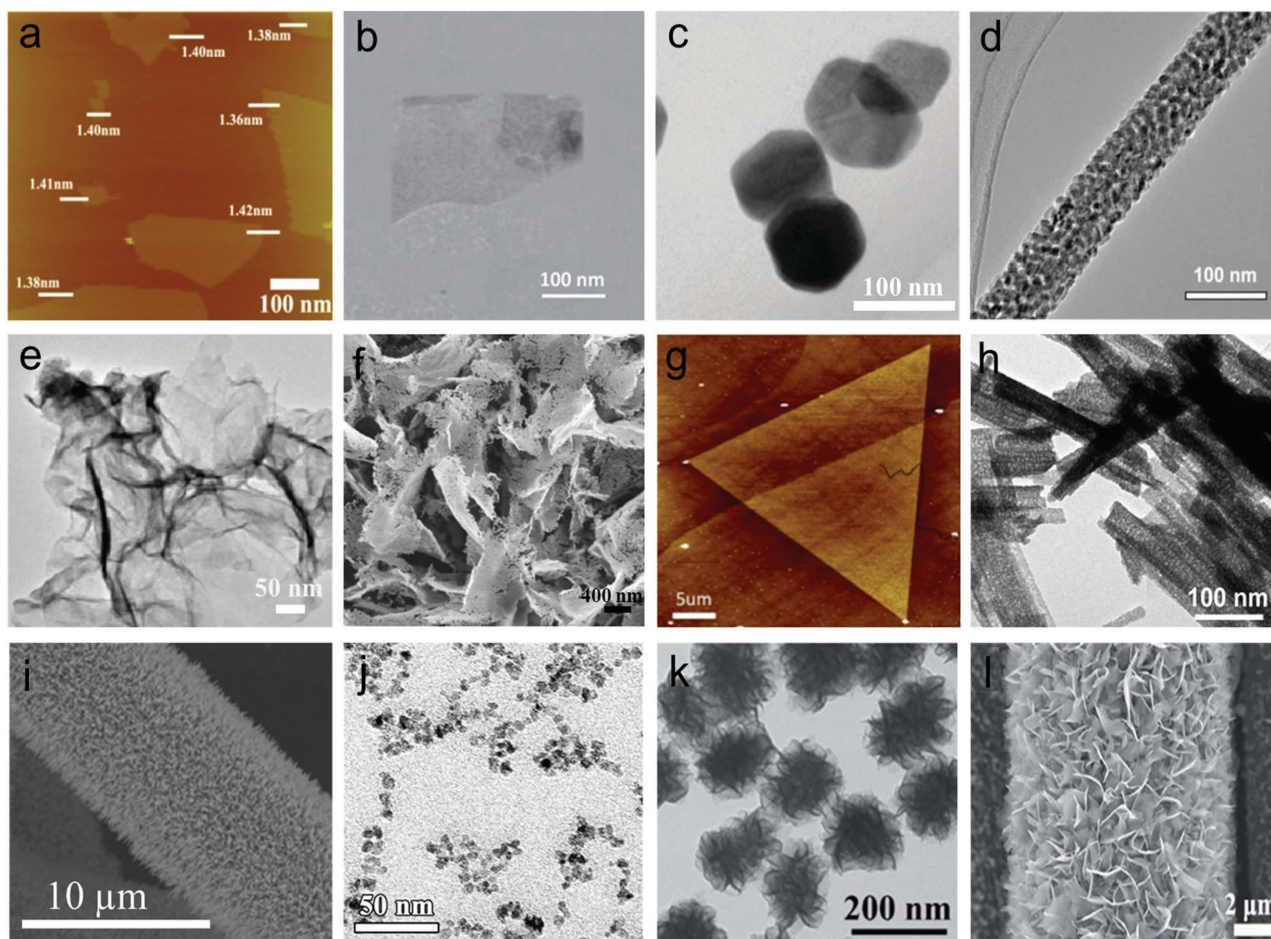


Figure 5. a) Atomic force microscopy (AFM) image of CoSe_2 nanosheets. Reproduced with permission.^[88] Copyright 2014, American Chemical Society. b) Transmission electron microscopy (TEM) image of the MoS_2 nanosheets. Reproduced with permission.^[103] Copyright 2016, Royal Society of Chemistry. c) TEM image of WSe_2 nanosheets. Reproduced with permission.^[76] Copyright 2016, Royal Society of Chemistry. d) TEM image of the reduced Co_3O_4 nanowires. Reproduced with permission.^[83] Copyright 2014, John Wiley & Sons, Inc. e) TEM image of the as-prepared $\text{Fe}_1\text{Co}_1\text{-O}$ nanosheets. Reproduced with permission.^[92] Copyright 2017, John Wiley & Sons, Inc. f) Scanning electron microscopy (SEM) image of Ar-plasma-engraved Co_3O_4 . Reproduced with permission.^[78] Copyright 2007, John Wiley & Sons, Inc. g) AFM image of a single crystalline MoS_2 monolayer flake after hydrogen plasma. Reproduced with permission.^[104] Copyright 2016, Elsevier. h) TEM image of WO_2 -carbon nanorods. Reproduced with permission.^[113] Copyright 2015, American Chemical Society. i) SEM image of CoO nanorods. Reproduced with permission.^[85] Copyright 2016, Nature Publishing Group. j) TEM image of Co_3O_4 nanoparticles. Reproduced with permission.^[89] Copyright 2016, American Chemical Society. k) TEM image of the hierarchical MoSe_{2-x} nanosheets. Reproduced with permission.^[77] Copyright 2014, Royal Society of Chemistry. l) SEM image of vertically oriented 3D $\text{Mo}(\text{S}_{0.53}\text{Se}_{0.47})_2$ nanosheets on carbon cloth. Reproduced with permission.^[102] Copyright 2016, Royal Society of Chemistry.

vacancies into tungsten selenide (WSe_2) nanosheets (Figure 5c) via reductive annealing treatment in Ar/H_2 of 95:5 volume ratio atmosphere.^[76] It is shown that selenium vacancies increase with annealing temperature up to 900 °C while the degree of structural disorder remains admissible. It is observed that the inert basal planes are activated due to the introduction of selenium vacancies, which provide the active sites for hydrogen adsorption to enhance the HER. Similar work of using reductive annealing has also been reported for the effective creation of oxygen vacancies in CaMnO_3 ^[75] and $\text{Ln}_2\text{Ti}_2\text{O}_7$ perovskites.^[111]

However, the annealing in the reducing atmosphere is unsuitable to process thermally unstable materials. Alternatively, a mild room-temperature aqueous reduction method involving reducing agents, e.g., sodium borohydride (NaBH_4), hydrazine (N_2H_4), can be employed. NaBH_4 has a strong

reductive capacity, which can release H_2 for reducing purpose. Zheng and co-workers used NaBH_4 to partially reduce Co^{3+} into Co^{2+} ions for the in situ generation of oxygen vacancies in mesoporous Co_3O_4 nanowires (Figure 5d) to enhance the OER performance.^[83] The mesopore feature facilitates fast mass transfer which enable efficient reduction treatment. Zhu and co-workers have observed that the reduction rates of iron-cobalt oxide nanosheets (Figure 5e) can be adjusted through the use of different reducing agents.^[92] They disclose that NaBH_4 shows a stronger and faster reducing capability than N_2H_4 , which ensures homogeneous dispersion of metal ions to deter the phase separation of different metals as such nanosheets' structure is preserved. This greatly benefits the generation of more oxygen vacancies in the $\text{Fe}_x\text{Co}_y\text{-O}$ nanosheets than the $\text{Fe}_x\text{Co}_y\text{-O}$ nanoparticles. Reduction by borohydride is a generic

and feasible approach to create vacancies in many other material systems, such as NiCo_2O_4 .^[97] Compared to the high-temperature reduction that demands higher energy input and imposes safety concerns, the wet chemical reduction strategy is comparatively cheaper, scalable, and convenient.

3.3. Plasma Etching

Plasma etching is a dry form of etching where the process gas converts the material to be etched from the solid to the gaseous phase (volatile etched products), which are then evacuated. The plasma etching introduces ion bombardment onto a nanocatalyst surface, where highly energetic ions transfer the energy to surface atoms by collisions which break the covalent bonds, leading to the ejection of the surface atoms to produce vacancies. Other than the physical etching, reactive gases such as O_2 and H_2 can bring about chemical plasma etching that triggers reactions of the gas radicals with surface atoms to effectively create vacancies. The few key parameters that affect the plasma etching process include pressure, flow rate, gas species, and excitation source.

Wang and co-workers have shown the creation of abundant oxygen vacancies on the Co_3O_4 nanosheets (Figure 5f) via a one-step Ar plasma treatment of 100 W, pressure 40 Pa for 60–240 s.^[78] The plasma treatment is reported to bombard the oxygen atoms out of the Co_3O_4 lattices and meanwhile reduces a part of Co^{3+} ions to Co^{2+} , thereby giving rise to oxygen vacancies. The same group has also demonstrated that the N_2 plasma treatment of higher plasma power (300 W) with similar pressure and irradiation time can simultaneously introduce heteroatom N doping and create oxygen vacancies in Co_3O_4 nanosheets.^[94] The doped N atoms that alter the electronic properties of the metal hosts, along with the abundant oxygen vacancies, are responsible for an OER enhancement. Other than single-type vacancies, plasma is capable of creating multiple vacancies.^[107] Oxygen and metal (Co and Fe) vacancies are introduced into monolayer CoFe LDH nanosheets through Ar plasma etching of 100 W under 0.2–0.4 Pa for 60 min.^[107] The low-pressure plasma etching compensated by the longer duration enables the breaking of the covalent bonds of the host layers in the lateral direction, facilitating the escape of surface metal and oxygen atoms from the lattice to produce multiple vacancies. These vacancies can effectively tune the electronic structures and increase the valence states of surrounding metal centers, hence contributing to higher OER activity. However, the structures of some ultrathin nanomaterials, such as the ultrathin Co_3O_4 ^[78,94] and MoS_2 nanosheets,^[112] are easily destroyed and decomposed into fragments by the plasma treatment due to the strong sputtering effect.

To mitigate the breakage issue and warrant the structural integrity, Li and co-workers have devised a remote hydrogen plasma strategy (20–50 W, 13 Pa for 30 min) that imposes mild plasma treatment on MoS_2 .^[84] The amorphous MoS_2 /carbon cloth sample is located at a remote position from the plasma coil to avoid direct plasma bombardment. The active hydrogen atoms/ions react with the sulfur atoms in MoS_2 to create sulfur vacancies. In addition, the same research group has also shown that high-density sulfur vacancies can be intro-

duced into the basal planes of monolayer crystalline MoS_2 (Figure 5g).^[104] They have successfully tuned MoS_2 with a wide range of atomic ratios from $\text{MoS}_{1.97}$ to $\text{MoS}_{1.20}$ using the same remote H_2 plasma technique to greatly enhance the HER performance. The plasma-mediated vacancies' creation approach is highly efficient as the whole process can be accomplished in minutes and moreover, precise plasma power, pressure, gas flow, and irradiation time can be fine-tuned to enable rich stoichiometry vacancies. However, the scalability of this technique is largely restricted by the high equipment cost of the plasma generator, vacuum, and power supply.

3.4. Thermal Treatment

Annealing at elevated temperatures leads to the loss of oxygen atoms in the case of metal oxides, thereby forming oxygen vacancies. Such thermal annealing is usually carried out in a vacuum system at a specific heating ramp rate and temperature under carrier gas, such as Ar, N_2 , O_2 , and air. The gas is introduced into the system at a constant flow rate to a desired pressure. The reaction temperature and pressure are held constant for a certain period to create vacancies, most probably, by the physical vaporization process. For materials that are easily oxidized, such as metal sulfides and selenides, thermal treatment can be conducted in an inert atmosphere, e.g., N_2 or Ar gas, in which sulfur and selenium vacancies can be created owing to the intrinsically higher volatility of the chalcogen atoms.

Zhang et al. have transformed the WO_3 /ethylenediamine hybrids into WO_2 -carbon mesoporous nanowires (Figure 5h) with a high concentration of oxygen vacancies via calcination in Ar gas at 700 °C for 5 h.^[113] During the annealing process, the N atoms in the ethylenediamine can extract the O atoms out of WO_3 to generate NO_x , thus giving rise to WO_2 with oxygen vacancies. Consequently, the WO_2 nanowires are rendered with metallic electronic structure as well as a large amount of active sites, which show high catalytic performance for HER. Xie and co-workers have prepared ultrathin NiCo_2O_4 nanosheets with rich and poor oxygen vacancies, which are realized by thermal transformation of Ni-Co/Co hydroxides in air and O_2 atmosphere at 300 °C, respectively.^[98] The escaping of O atoms from the lattices could be retarded owing to the high density of surrounding O_2 gas, therefore generating fewer oxygen vacancies.

In addition to the gas atmosphere, other conditions such as temperatures can also be tuned to manipulate the vacancies. Ling et al. have reported that cation exchange temperatures can considerably affect the concentration of the generated oxygen vacancies of 1D single-crystal cobalt oxide (CoO) nanorods (Figure 5i).^[85] The temperature ranging from 600, 650, to 700 °C for 30 min under Ar gas has shown to vary the composition of CoO_x ($x = 0.97, 0.91, \text{ and } 0.82$), which corresponds to oxygen vacancies of 0.03, 0.09, and 0.18. It is evident that the higher exchange temperature supports the formation of increasing oxygen vacancies. However, it is noteworthy that the high temperature damages the structural features and decreases the electronic conductivity as well as electrocatalytic activity of the CoO. This is in agreement with other reported works where the presence of excessive oxygen defects induces adverse structural instability and electronic conductivity.^[80,114,115] Despite the

requirement of elevated temperature and controlled gas flow, the fairly straightforward thermal treatment is able to process materials of high throughput, showing great potential for large-scale applications. Unlike the plasma etching route, thermal treatment is less stringent on specific equipment setup and requirement, hence providing an easier and cheaper access to create vacancies in a nanocatalyst system.

3.5. Other Methods

Apart from the above-mentioned methods, there are other means of creating vacancy-constituted nanocatalysts. Laser fragmentation has been employed to rapidly form fine Co_3O_4 nanoparticles (Figure 5j) that are rich in oxygen vacancies. The entire process is realized using a nanosecond pulsed neodymium-doped yttrium aluminum garnet (Nd:YAG) laser (power density of $6 \times 10^7 \text{ W cm}^{-2}$) in 20 min at room temperature.^[89] The high-temperature and -pressure laser ablation of an ideal fluence of 0.6 J cm^{-2} with rapid heat quenching process assists the formation of oxygen vacancies. This method is likely a physical process without the need of chemical precursors or surfactants, contributing to a clean exposed surface with high reactivity. Another more scalable technique of producing vacancies involves the electrochemical desulfurization. It has been reported that sulfur atoms in the basal plane of MoS_2 can be electrochemically reduced and removed as H_2S gas. Consequently, stabilized clusters of sulfur vacancies are formed.^[73] Changing the voltages between -2.0 and 0.0 V (vs RHE) can vary the degree of desulfurization, resulting in different densities of active sites to tune the HER activity. It is also anticipated that the electrochemical reduction could, in principle, be used to create vacancies in sulfide, selenide, and phosphide materials.

A few bottom-up approaches that also work perfectly to create desired vacancies in the electrocatalysts have been reported, such as hydrothermal and CVD. Distinct from the top-down approaches that mostly involve postactivation of electrocatalysts, the bottom-up methods offer the advantage of creating built-in vacancies during the crystal growth, which enables the production of large homogeneous vacancy-enriched nanocatalysts. For instance, Yang and co-workers have reported a simple bottom-up colloidal synthesis approach to create selenium vacancies on ultrathin MoSe_{2-x} nanosheets (Figure 5k).^[77] The process can be completed within 20 min to avoid long reaction time and expensive equipment cost. Of note, this colloidal reaction pathway could also be expanded to synthesize ultrathin WSe_2 , SnSe , and PbSe nanosheets,^[77] demonstrating the universality of the strategy. Moreover, a bottom-up gas-phase CVD method has been used to grow vertically oriented 3D $\text{MoS}_{2(1-x)}\text{Se}_{2x}$ alloy nanosheets on carbon cloth (Figure 5l) with both sulfur and selenium vacancies, arising from the introduction of different proportions of sulfur and selenium powders into MoO_3 precursors.^[102] Although performed at atmospheric pressure, this CVD process requires high temperature of $650\text{--}850 \text{ }^\circ\text{C}$ for $10\text{--}30 \text{ min}$ and high purity Ar gas flow to keep out oxidation of the material.

In brief, vacancies can be created in the electrocatalysts during the material synthesis or post-treatment using various

techniques, and can be further engineered by tuning synthetic or processing conditions. The advantages and disadvantages of different approaches have been briefly discussed, in which the effectiveness, complexity, operation, cost, and safety should be taken into consideration. Moreover, the development of new techniques that focus on creating different types of vacancies and precisely controlling the density and distribution of vacancies is essential for enhancing the electrocatalytic performances.

4. Advanced Characterizations of Functional Vacancies

After the intentional creation of vacancies in the nanocatalysts, it is necessary to identify and study these vacancies using advanced measurement and characterization tools down to the atomistic level. Cutting edge microscopy and imaging techniques have been developed to examine the micro/nanostructures, local coordination atoms, and electronic structures/states of the vacancy-rich transition-metal-based electrocatalysts. In the following section, a few representative examples are used to illustrate the indispensable characterization techniques that can provide an in-depth understanding, insight, and quantification of the nanocatalyst vacancies. We will highlight and compare these commonly used complementary techniques.

4.1. X-Ray Photoelectron Spectroscopy

X-ray photoelectron spectroscopy (XPS) is a surface-sensitive spectroscopic technique that is widely used to analyze the elemental composition and chemical state, as well as provide quantitative information of the elements within a material.^[116] In the vacancy-rich nanocatalysts, the presence of vacancies would alter the electronic structure and chemical environment of the elements in the materials, which affects the bonding energies and results in the change of XPS spectrum, including peak shift, intensity variation, or the generation of new XPS peaks. Xie and co-workers have prepared ultrathin oxygen vacancy-rich NiCo_2O_4 nanosheets for enhanced electrochemical H_2O oxidation.^[98] The deficiency of oxygen in the as-obtained ultrathin nanosheets and the corresponding bulk samples have been studied by XPS. As displayed in Figure 6a, the O 1s core level spectra present three identified peaks. The main O1 peak located at 529.7 eV is a typical lattice oxygen (O^{2-}) for metal–oxygen bonds, whereas the O2 peak at 531.2 eV is attributed to a high number of defect sites with low oxygen coordination and the O3 peak at 532.6 eV is associated with hydroxyl species of surface-adsorbed water molecules. The large deconvoluted O2 peak area indicates the existence of abundant oxygen vacancies.

In addition, the characterization of sulfur/selenium vacancies in metal sulfide/selenide nanocatalysts has also been realized by XPS analysis.^[73,74,76,77,84,104] In a recent contribution, Zheng and co-workers have introduced a scalable generation of sulfur vacancies on the 2H- MoS_2 basal plane by selective removal of S atoms.^[73] As presented in Figure 6b, the S 2p peaks for vacancy-rich MoS_2 (V- MoS_2) are much weaker than those of pristine MoS_2 (P- MoS_2), indicating the removal

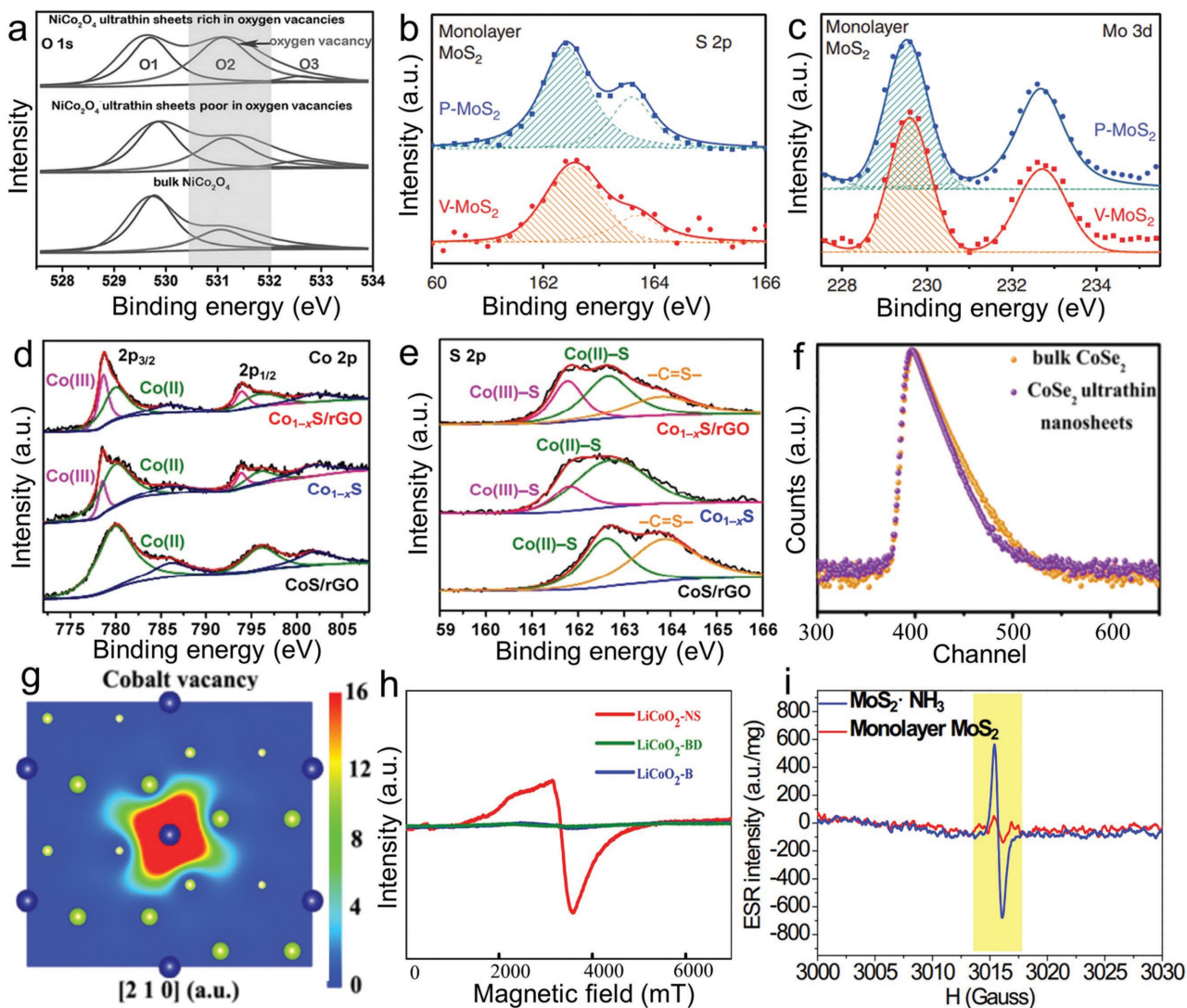


Figure 6. a) O 1s XPS spectra of the different NiCo_2O_4 samples. Reproduced with permission.^[98] Copyright 2015, John Wiley & Sons, Inc. b) S 2p and c) Mo 3d XPS peaks of pristine MoS_2 (P- MoS_2) and MoS_2 with sulfur vacancies (V- MoS_2). Reproduced with permission.^[73] Copyright 2017, Nature Publishing Group. d) Co 2p and e) S 2p XPS spectra of $\text{Co}_{1-x}\text{S}/\text{rGO}$, Co_{1-x}S , and CoS/rGO . Reproduced with permission.^[87] Copyright 2017, Springer. f) Positron lifetime spectrum of ultrathin CoSe_2 nanosheets with vacancies and bulk CoSe_2 ; g) schematic representations of trapped positrons of cobalt vacancies. Reproduced with permission.^[88] Copyright 2014, American Chemical Society. h) EPR spectra of LiCoO_2 -NS, partially delithiated bulk LiCoO_2 sample (LiCoO_2 -BD), and LiCoO_2 -B. Reproduced with permission.^[91] Copyright 2017, American Chemical Society. i) EPR spectra of bulk MoS_2 and sulfur vacancy-rich monolayer MoS_2 . Reproduced with permission.^[103] Copyright 2016, Royal Society of Chemistry.

of sulfur atoms and creation of vacancies during the desulfurization process. In contrast, the Mo 3d peaks of P- MoS_2 and V- MoS_2 are similar (Figure 6c), suggesting that the Mo atoms are not significantly affected. Moreover, through the normalization of S 2p spectrum using Mo 3d intensities, the S:Mo peak area ratio for V- MoS_2 is about 25% smaller than that of P- MoS_2 with the atomic ratio of 2.0, indicating the sulfur vacancies ratio for V- MoS_2 is about 25%.

Apart from the detection of anion vacancies, the XPS analysis has been further demonstrated to be efficient for studying cation vacancies. Ren and co-workers have designed an Co-deficient $\text{Co}_{1-x}\text{S}/\text{reduced graphene oxide (rGO)}$ electrocatalyst for high-efficiency OER.^[87] For comparison, the Co_{1-x}S and the CoS/rGO hybrid have also been prepared and studied.

Initially, the atomic ratio of cobalt to sulfur in the $\text{Co}_{1-x}\text{S}/\text{rGO}$ hybrid was calculated to be $\approx 0.81:1$, which is much lower than that in Co_{1-x}S (0.87:1) and CoS/rGO (0.95:1). Moreover, the high-resolution Co 2p spectra of $\text{Co}_{1-x}\text{S}/\text{rGO}$ hybrid and Co_{1-x}S show new peaks at 780.3 and 796.3 eV assigned to Co^{III} (Figure 6d), which are absent in the spectrum of the CoS/rGO . The presence of Co^{III} in the $\text{Co}_{1-x}\text{S}/\text{rGO}$ hybrid and Co_{1-x}S is attributed to the formation of cobalt vacancies, which leads the neighboring S atoms to share their electrons. Moreover, a peak at 161.75 eV originating from $\text{Co}^{\text{III}}-\text{S}$ is also observed in the S 2p XPS of the $\text{Co}_{1-x}\text{S}/\text{rGO}$ hybrid and Co_{1-x}S (Figure 6e). The easily accessible XPS technique has the merits of good precision and accuracy, and sensitive to a variety of elements. It is thus far the most commonly used

technique for the characterization and study of vacancy-rich nanocatalysts.

4.2. Positron Annihilation Spectroscopy

Positron annihilation spectrometry (PAS), sometimes referred to as positron annihilation lifetime spectroscopy, is also a well-established technique to study the defects in solids.^[117,118] The utilization of the PAS technique for studying vacancies is mainly based on the following two principles: (i) positrons are antiparticles to electrons. The positrons injected into a solid will annihilate with electrons and emit energy as annihilation gamma rays, which hold information about the electronic environment around the annihilation site; (ii) the vacancies can trap positrons and change the annihilation characteristics such as the lifetime of the positron, which makes it possible to distinguish a sample containing vacancies from a defect-free one.^[118,119] Thus, measuring the positron lifetime can give information about the type and relative concentration of vacancies in a solid material, even at the parts-per-million level.

Xie and co-workers have prepared a cobalt vacancy-rich ultrathin CoSe₂ nanosheets and studied the vacancies by PAS,^[88] as shown in Figure 6f. The positron lifetime spectra of both CoSe₂ ultrathin nanosheets and bulk CoSe₂ can be fitted by an exponential function of three distinct lifetime components, τ_1 , τ_2 , and τ_3 , with relative intensities I_1 , I_2 , and I_3 . The two τ_2 and τ_3 components with longer lifetime can be assigned to the large defect clusters and the interface presented in the material, respectively. The shortest component (τ_1) can be attributed to the trapped positron annihilation by cobalt vacancies (Figure 6g). In addition, further information about the relative concentration of the vacancies can be obtained by the relative intensity (I) of the positron. The highest intensity of τ_1 of ultrathin CoSe₂ nanosheets indicates that cobalt vacancies are predominant in this sample.

In addition, Jin and co-workers have adopted the PAS technique to study the MoS₂ nanosheets with abundant sulfur vacancies.^[101] They reported similar positron lifetime spectra with three lifetime components, corresponding to the annihilations at the bulk, sulfur vacancies, and MoS₂ voids/surface, respectively. They also found that the higher sulfur vacancies results in higher intensity of I . This can be ascribed to that the positron lifetime which is inversely proportional to the electron density encountered by the positron.^[120] Owing to the fact that the average electron density at the vacancies is lower than that in the bulk, consequently, the lifetime of the trapped positron is increased compared to the value in the perfect bulk lattice.

In short, the PAS technique is a well-established technique to probe the size, type, and relative concentration of various defects/vacancies on an atomic scale.^[117,121] Moreover, since the annihilation characteristics of PAS can be calculated from first principles, the PAS technique is strongly supported by theory, which can substantially facilitate the analysis and interpretation of data measured by PAS. In these regards, more attention can be devoted to this technique.

4.3. Electron Paramagnetic Resonance Spectroscopy

Electron paramagnetic resonance (EPR) spectroscopy, also known as electron spin resonance spectroscopy, is another effective method for the characterization of vacancy-rich nanocatalysts. This technique is based on the absorption of microwave radiation by unpaired electrons when it is exposed to a strong magnetic field.^[122] Since the generation of vacancies is normally accompanied by broken or missing of chemical bonds, the nanocatalysts with vacancies would have considerable unpaired electrons and present typical EPR signals.

Taking the metal oxide materials as an example, the deficiency of oxygen has been well demonstrated to induce a characteristic EPR peak at the position of about $g = 2.0$, and the EPR signal intensity is positively correlated with the vacancies amount. For instance, Li and co-workers have reported an ultrathin LiCoO₂ nanosheets (2–3 nm) with abundant oxygen vacancies for OER.^[91] They have proven that the ultrathin LiCoO₂ nanosheets (LiCoO₂-NS) display a strong signal at about $g = 2.0$ in the EPR spectrum, which is attributed to the single-electron-trapped oxygen vacancies. In contrast, the counterpart samples of bulk LiCoO₂ (LiCoO₂-B) and partially delithiated bulk LiCoO₂ (LiCoO₂-BD) with negligible vacancies show no obvious peak at the position, as presented in Figure 6h.

Besides the detection of oxygen vacancies, the EPR analysis has also been applied to characterize the sulfur vacancies. Luo and co-workers have synthesized a monolayer 2H phase MoS₂ nanosheets with a large concentration of sulfur vacancies.^[103] As shown in Figure 6i, a signal at about 3015 G is observed in both the MoS₂·NH₃ precursor and monolayer MoS₂ samples. Notably, this peak is ascribed to the contribution from Mo–S dangling bonds rather than the sulfur vacancies. A higher intensity indicates less sulfur vacancies. Therefore, the monolayer MoS₂ with abundant sulfur vacancies reveals an obvious decrease of signal intensity compared to the MoS₂·NH₃ counterpart. A similar phenomenon has also been observed in the work of Jin and co-workers.^[101] They have synthesized a mesoporous metallic 1T phase sulfur-deficient MoS₂ nanosheet. The generation of large concentration of sulfur vacancies in the 1T MoS₂ sample significantly decreases the S signal in comparison with pristine bulk MoS₂. It is notable that EPR detection of sulfur vacancies is different from the aforementioned case for the detection of oxygen vacancies, in which the signal is generated from the vacancies and its intensity increases with the vacancies' content.

At present, the EPR technique for the study of vacancy-rich nanomaterials in electrocatalysis mainly focuses on the detection of oxygen and sulfur vacancies. The report of identifying other vacancies such as cation vacancies with this technique is rare. However, it should be noted that the EPR technique is sensitive for the study of a variety of cations, e.g., Co, Fe, Ni, and Mn,^[123–126] which are typical constituents of transition-metal-based electrocatalysts.

4.4. X-Ray Absorption Fine Structure Spectroscopy

Besides the above techniques, recently, synchrotron-based atomic X-ray absorption fine structure (XAFS) spectroscopy has

also been extensively adopted to characterize vacancies. Typically, the XAFS spectrum includes two regimes: X-ray absorption near-edge spectroscopy (XANES) and extended X-ray absorption fine-structure spectroscopy (EXAFS). The XANES is exceptionally sensitive to oxidation state and coordination chemistry (e.g., octahedral and tetrahedral coordination) of the absorbing atom, while the EXAFS is used to determine the distances, coordination number, and species of the neighbors.^[127] Collectively, the XAFS provides a powerful element-specific tool to study the local atomic geometry and the chemical state of the atoms for a specific constituent element in a material.

The existence of vacancies would strikingly change the local chemical and electronic environment of the atoms in materials, which is reflected as obvious XAFS spectral change. The XAFS has been generically used to detect various vacancies including metal and nonmetal in the nanocatalysts.^[76,88,91,105,107,108,128,129] Zhang and co-workers have synthesized an ultrathin δ -MnO₂ nanosheets electrocatalyst (≈ 1.4 nm, denoted as NS-MnO₂) with abundant oxygen vacancies for overall water splitting.^[79] The local atomic structure around Mn with deficient oxygen has been studied by XAFS. **Figure 7a** shows the Mn K-edge XANES spectra of bulk-MnO₂ and NS-MnO₂, which discloses that the absorption edge of NS-MnO₂ shifts by about 0.5 eV to lower energy than that of bulk-MnO₂, implying a slightly lower oxidation state of Mn in the NS-MnO₂ sample. In addition, the Mn K-edge EXAFS $k^2\chi(k)$ oscillation curve of the ultrathin NS-MnO₂ displays a noticeable amplitude difference in comparison with that of the bulk-MnO₂ (Figure 7b), which indicates

that the local atomic arrangements of Mn atoms in the two samples are different. The Fourier transformation of EXAFS data further supports the analysis. As shown in Figure 7c, the two main peaks in *R*-space spectra correspond to the first Mn–O and Mn–Mn shells, respectively. The weaker intensities of these peaks for NS-MnO₂ reveal reduced Mn–O coordination number (4.9) and Mn–Mn coordination number (5.4) compared to the corresponding values for bulk-MnO₂ (both 6.0). These results provide solid evidence for the existence of oxygen vacancies in NS-MnO₂.

The XAFS spectroscopy reveals the details of how X-rays are absorbed by an atom at energies near and above the core-level binding energies of that particular atom. It allows direct detection of chemical and physical states of the nanocatalyst vacancy systems, which needs to be accompanied by rigorous data analysis for factual interpretation. Essentially, the XAFS technique can be used to atomically probe any element vacancies based on the core-level electrons.

4.5. High-Angle Annular Dark-Field Scanning Electron Microscopy

From the above discussion, the techniques including XPS, PAS, EPR, and XAFS are all effective for the characterization of vacancies. Nonetheless, these techniques for the analysis of vacancies are based on the spectral analysis and normally regarded as nonvisual type. In order to visually distinguish the

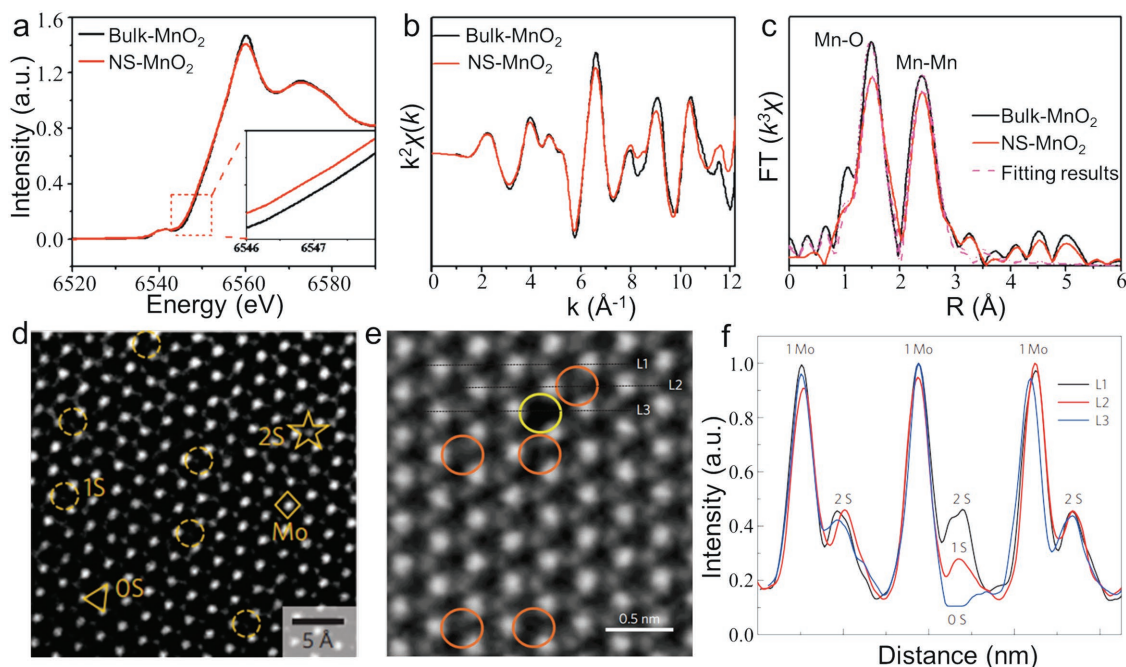


Figure 7. a) Mn K-edge XANES spectra, b) Mn K-edge EXAFS oscillation function $k^2\chi(k)$, and c) magnitude of k^2 -weighted Fourier transforms of Mn K-edge EXAFS spectra for Bulk-MnO₂ and NS-MnO₂ (vacancy-rich). Reproduced with permission.^[79] Copyright 2017, John Wiley & Sons, Inc. d) ACTEM image of a 4×4 nm² MoS₂ monolayer with about 43 sulfur vacancies ($\approx 11.3\%$ sulfur vacancy). Reproduced with permission.^[74] Copyright 2016, Nature Publishing Group. e) STEM image of a single-layer CVD-grown MoS₂ nanosheet with different types of vacancies single sulfur vacancy (orange circles) and double sulfur vacancy (yellow circles); f) intensity profiles along lines L1–L3. Higher contrast is obtained from the Mo atoms compared to one sulfur atom ($\approx 30\%$ of the Mo intensity) and two sulfur atoms ($\approx 45\%$ of the Mo intensity). In the absence of sulfur atoms (L3), the intensity decreases to $<10\%$. Reproduced with permission.^[130] Copyright 2016, Nature Publishing Group.

vacancies, transmission electron microscopy (TEM) technique, specifically aberration-corrected TEM (ACTEM), has shown remarkably improved signal-to-noise ratio, resolution, and sensitivity for precise calculation of vacancies' concentration. In the high-angle annular dark field scanning mode TEM (HAADF-STEM), the illumination aberration corrector reduces coherent aberration effect on the electron probe and increases the probe convergence angle such that nanocatalyst vacancies' analysis for both lateral and depth resolution can be improved.

Zheng and co-workers have recently reported an Ar plasma-induced creation of sulfur vacancies on monolayer 2H-MoS₂ basal planes and employed ACTEM to directly study the sulfur vacancies.^[74] As shown in Figure 7d, the image shows that the Ar-plasma-treated MoS₂ contains four types of spots with different brightness, in which the biggest and brightest spots (rhombus) are Mo atoms, while the small bright dots (star), small dim dots (circle), and dark spots (triangle) correspond to a pair of S atoms (2S, one S atom above and the other below the Mo plane), a single S atom (1S, only one S atom below the Mo plane), and zero S atoms (0S, both top and bottom S atoms removed), respectively. The missing of the S atoms (one or two) and absence of Mo removal confirm the successful formation of sulfur vacancies. In addition, the size of the ACTEM image is 4 × 4 nm² MoS₂ monolayer. By counting the number of the Mo atoms (190) and those sulfur vacancies (43) with dimmer or absent brightness (43), the percentage of sulfur vacancies is calculated to be ≈11.3%. Following the same way, the average sulfur vacancies' percentage over ten such areas is 12.5% ± 2.5%, which is consistent with the 13.0% ± 2.0% sulfur vacancies estimated by XPS.

Moreover, Chhowalla and co-workers have also reported direct observation of sulfur vacancies in a single-layer CVD-grown MoS₂ nanosheet through HAADF-STEM owing to the contrast obtained by the presence and the nature of the atoms under the electron beam.^[130] As shown in Figure 7e, single sulfur vacancy (orange circles) and double sulfur vacancy (yellow circles) are naturally present in the samples. Figure 7f shows the intensity profiles along lines L1–L3. The contrast is in accordance with the HAADF-STEM analysis, further supporting the presence of single and double sulfur vacancies. Furthermore, a careful analysis of the MoS₂ basal plane in large area (>500 nm²) has also been carried out, which reveals that the large majority of the defects consist of single sulfur vacancies with a density of the defects of up to ≈9%. With unmatched spatial and temporal resolution, STEM coupled with electron energy loss spectroscopy can be used to provide indisputable visualization, quantification, and identification of the vacancies. More information on the exact location, distribution, depth, lattice distortion, chemical composition can be further derived.

To sum up, the above-discussed techniques are the most commonly used ones to study functional vacancies in electrocatalysts. Generally, two or more of the complementary techniques are combined to confirm the presence and identify the type of vacancies. Moreover, apart from these techniques, some other in situ or operando characterization techniques such as synchrotron-based X-ray diffraction, hard X-ray microscopy, nuclear magnetic resonance, mass spectroscopy, and Raman spectroscopy also offer reliable and invaluable mechanistic fundamental, real-time monitoring, and evolution studies of vacancies,

especially important in guiding future defects design and optimization.

5. Correlations between Vacancies and Electrochemical Activities

Many works have already established clear correlation and corroborative influence of vacancies on electrochemical OER and HER performance. Consequently, precise control of vacancies and more comprehensive understanding on various catalyst systems' research have flourished. In this section, the predominant effects of vacancies on modulation of active sites' density, electrical conductivity, and kinetic energy barriers of water splitting are primarily highlighted.

5.1. Modulating the Density of Active Sites

In general, the catalytic performances (OER and HER) of the electrocatalysts are lower than expected, which is restricted by the lack of active sites. Vacancies at atomic level give rise to unsaturated coordination and modified electronic structures, which have been demonstrated to largely augment the number of accessible active sites. Consequently, the overall density of active sites in nanocatalysts along with the electrocatalytic activities can be significantly improved.

Taking the most well-studied layered transition-metal chalcogenide MoS₂ as an example, various experimental and computational studies have shown that the creation of sulfur vacancies generates new catalytic sites and increases the active site density in the MoS₂ nanosheets.^[73,74,84,101,103] Zheng and co-workers have introduced sulfur vacancies and strain in the basal plane to enhance the HER performance of monolayer 2H-MoS₂ (Figure 8a).^[74] Their theoretical and experimental results show that the sulfur vacancies in the basal plane of 2H-phase monolayer MoS₂ act as new highly active and tunable catalytic sites for HER. The mechanism has been proposed to that the creation of vacancies introduces new gap states around the Fermi level (Figure 8b), which allows favorable hydrogen adsorption on the sulfur vacancies. At a certain range of density of sulfur vacancies, the hydrogen bond to the catalyst surface is neither too strong nor too weak, which is beneficial for HER. Moreover, it is noteworthy that this work has also revealed that further application of external strain on the sulfur vacancy-rich MoS₂ can shift the positions of the vacancy-induced new bands toward the Fermi level, resulting in a narrowing bandgap and increasing number of gap states around the Fermi level (Figure 8c). As a result, the adsorption strength on the sulfur vacancy sites can increase and thus further optimize the HER performance of vacancy-rich MoS₂. In a subsequent work of Zheng and co-workers,^[131] they revealed that the strained S vacancy has an electron-transfer rate four times higher than that of the unstrained S vacancy, confirming that the tensile elastic strain accelerates the HER kinetics of sulfur vacancies in MoS₂. Therefore, these works unambiguously demonstrate that the creation of vacancies can induce new catalytic sites, while the applied strain can further "activate" the generated catalytic sites and boost the reaction kinetics. The creation and straining of

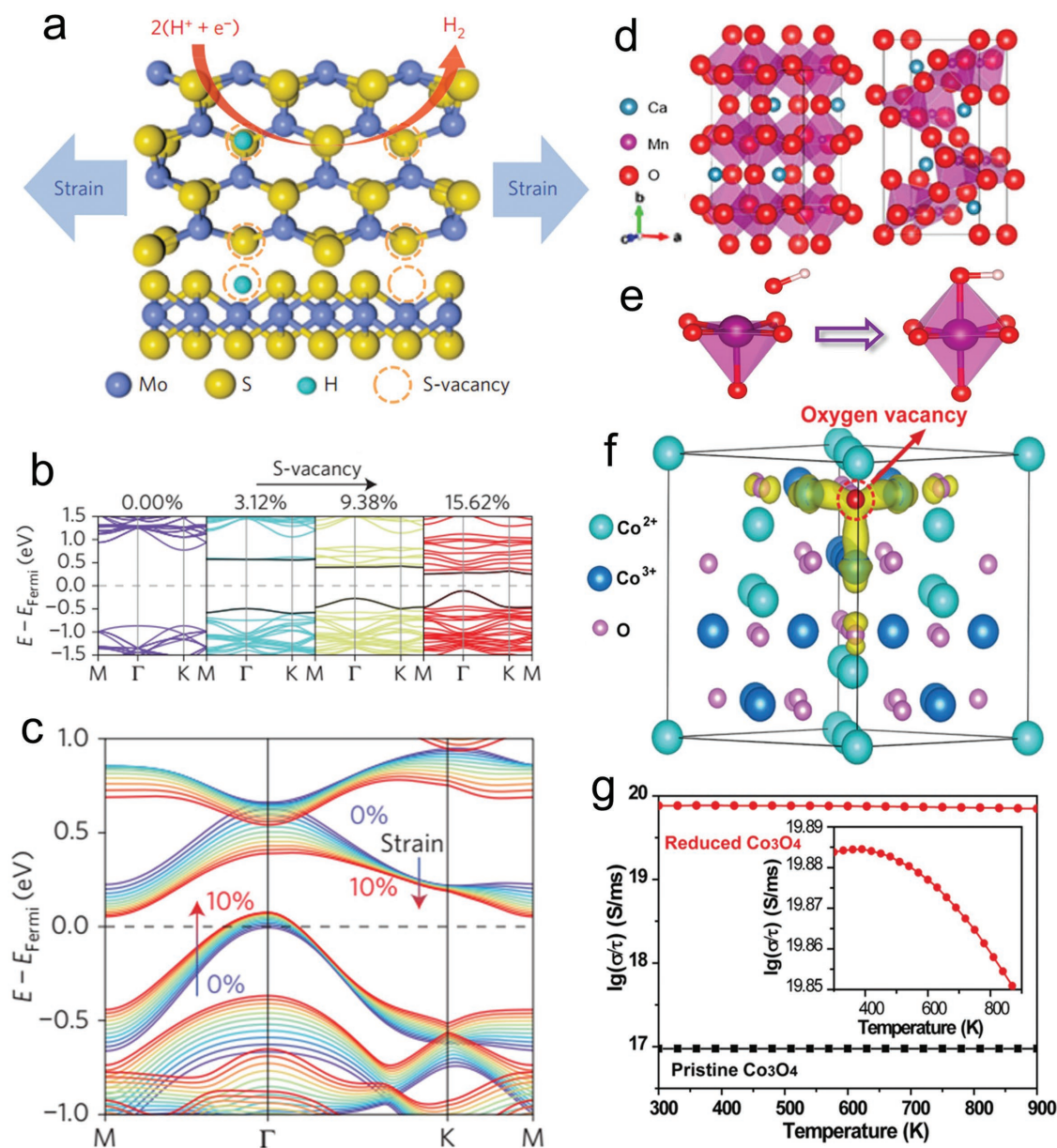


Figure 8. a) Schematic of the top (upper panel) and side (lower panel) views of MoS₂ with strained sulfur vacancies on the basal plane, where sulfur vacancies serve as the active sites for hydrogen evolution and applied strain further tunes the HER activity; b) tuning of the band structure due to increasing S-vacancy concentrations (calculated using the full 4×4 unit cell); c) fine-tuning of the band structure for 25% S-vacancy under applied strain. Reproduced with permission.^[74] Copyright 2016, Nature Publishing Group. d) Unit cell structures of CaMnO₃ (left) and Ca₂Mn₂O₅ (right); e) illustration of possible effect of oxygen vacancies in the Ca₂Mn₂O₅ crystal structure on oxygen evolution kinetics. Reproduced with permission.^[75] Copyright 2014, American Chemical Society. f) Partial charge density of the reduced Co₃O₄ obtained from DFT calculation (oxygen vacancy-rich) (the states of Co^{2+} are displayed in yellow and the iso-surface levels are $0.037 \text{ e}\text{\AA}^{-3}$); g) calculated conductivity for the reduced Co₃O₄ and the pristine Co₃O₄ (inset shows an expansion of the plot of reduced Co₃O₄). Reproduced with permission.^[83] Copyright 2014, John Wiley & Sons, Inc.

sulfur vacancies display different functions but synergistically enhance the performance of vacancy-rich electrocatalysts, which can be combined as a general way of constructing new highly efficient electrocatalysts.

Similarly, Li and co-workers have also reported the proliferated active site density in amorphous MoS₂ by the creation of sulfur vacancies. Their study reveals that when vacancies are created on MoS₂, a bound state is generated slightly below the Fermi level.^[84] This state is responsible for hydrogen adsorption on the

sulfur vacancies, which can activate the H₂ evolution, and thus enhance the HER activity of MoS₂. This conclusion is consistent with the previous report.^[74] Moreover, selenium and sulfur elements belong to group (VI) chalcogen. Thus, in the reported selenium vacancy-rich metal selenides, the selenium vacancies have been reported to display a similar role as that of sulfur vacancies. This has been demonstrated in the selenium vacancy-rich exfoliated WSe₂^[76] and MoSe_{2-x}^[77] nanosheets. The studies validate that the selenium vacancies in MSe₂ (M = Mo and W) act as new

catalytic sites, which improves the active sites' density and thus enhances the catalytic performance of MSe_2 .

Besides acting as new catalytic sites directly, another important way for improving the active sites' density through the introduction of vacancies is to promote the generation/exposure of metal active sites. For instance, Yang and co-workers have prepared a pure phase perovskite oxygen-deficient $\text{Ca}_2\text{Mn}_2\text{O}_5$ with square pyramid MnO_5 subunit by removing the lattice oxygen from perovskite CaMnO_3 with octahedral MnO_6 subunit (Figure 8d).^[75] They have demonstrated that the removal of oxygen atoms from CaMnO_3 remarkably modifies the unit cell structure, electron configuration on manganese, and results in the chemical transformation of $\text{Ca}_2\text{Mn}_2\text{O}_5$. This modification has been illustrated as (i) the oxygen-deficient $\text{Ca}_2\text{Mn}_2\text{O}_5$ contains a unique square pyramid MnO_5 subunit with a zigzag structure, which gives ordered oxygen vacancies and the molecular level oxygen porosity beyond the mesoscale porosity, thus favoring the facile transport of OH^- ; (ii) the larger ion radius of Mn^{3+} (0.645 Å) in $\text{Ca}_2\text{Mn}_2\text{O}_5$ than Mn^{4+} (0.53 Å) in CaMnO_3 induces a more distorted structure and larger cell volume in $\text{Ca}_2\text{Mn}_2\text{O}_5$, facilitating OH^- ion uptake into the oxygen vacant sites. Meanwhile, the Mn^{3+} ($3d^4$) in $\text{Ca}_2\text{Mn}_2\text{O}_5$ gives $t_{2g}^3 e_g^1$ electron configuration (the high-spin state on manganese), which can easily forms bonding structure with OH^- (Figure 8e), leading to the formation of intermediate of OH^- - MnO_5 octahedral unit. The moderate bonding strength by overlapping of two orbitals (e_g orbital on Mn^{3+} and the $\text{O}-p_\sigma$ orbital on OH^-) can facilitate the ion exchange of O^{2-} and O_2^{2-} , which is the rate-determining step in the OER process. These factors collectively lead to a fast OER kinetics and high activity of oxygen vacancy-rich $\text{Ca}_2\text{Mn}_2\text{O}_5$.

This vacancy-induced generation/exposure of active sites has also been reported in other vacancy-rich nanocatalysts such as Co_3O_4 and MnO_2 .^[78,79] Zhang and co-workers reported the oxygen vacancy-engineered ultrathin δ - MnO_2 nanosheet arrays for overall water splitting.^[79] They disclose that abundant oxygen vacancies in δ - MnO_2 nanosheets lead to the increased exposure of Mn^{3+} active sites. The HER and OER are envisaged to proceed via the oxidation of Mn^{3+} to Mn^{4+} (i.e., $\text{Mn}^{3+} + \text{H}_2\text{O} \rightarrow \text{Mn}^{4+} + 1/2\text{H}_2 + \text{OH}^-$) and reduction of Mn^{3+} to Mn^{2+} ($4\text{Mn}^{3+} + 4\text{OH}^- \rightarrow 4\text{Mn}^{2+} + \text{O}_2 + 2\text{H}_2\text{O}$), respectively. Thus, the abundance of oxygen vacancies in MnO_2 nanosheets creates and stabilizes the active Mn^{3+} sites, and ultimately underpins the excellent overall water-splitting performance. Therefore, it is concluded that creating vacancies activates new catalytic sites and/or promotes the exposure of active sites. Accordingly, the catalytic performance with augmented reaction sites by the introduction of vacancies will exceed that of the pristine catalyst.

5.2. Tuning the Electrical Conductivity

In addition to the lack of active sites, poor electrical conductivity is another dominant factor that suppresses the electrochemical water-splitting performance of transition-metal-based nanocatalysts. The electrical conductivity of nanocatalysts is strongly correlated with the charge transfer, which plays a key role in the electrochemical reaction (OER and HER) kinetics. High

electrical conductivity could facilitate the charge separation and transfer, thus accelerating the rate of the water splitting and lowering the overpotential efficiently. Introducing vacancies has been proven to enhance the conductivity of the electrocatalysts, hence promoting the activity of the electrochemical reactions.

Zheng and co-workers have reported an improved conductivity of oxygen vacancy-rich Co_3O_4 compared to its pristine counterpart.^[83] Density functional theory (DFT) calculations show that the presence of oxygen vacancies results in the formation of a new gap state within the bandgap of Co_3O_4 . The two electrons that previously occupy oxygen 2p orbitals become delocalized around the three Co^{3+} atoms neighboring the oxygen vacancy, as well as the adjacent O atoms (Figure 8f). This induces a much higher degree of electron delocalization in the reduced vacancy-rich Co_3O_4 than the pristine one. The electrons in the delocalized electronic structure are calculated to be easily excited into the conduction band, leading to an enhanced electrical conductivity (Figure 8g). Similar conclusions have been drawn in the works of oxygen vacancy-rich Co_3O_4 nanosheets and oxygen-deficient Co_3O_4 nanoparticles, reported by Wang and co-workers^[78] and Du and co-workers,^[89] respectively. They have also demonstrated the conductivity of Co_3O_4 can be improved by introducing oxygen vacancies, which ensures good charge separation and transport, beneficial for high electrocatalytic performance.

Other than that, Chen and co-workers have synthesized a series of nonstoichiometric perovskite $\text{CaMnO}_{3-\delta}$ for OER.^[80] The moderate oxygen-defective $\text{CaMnO}_{2.75}$ with one oxygen vacancy per unit cell displays a much higher electrical conductivity than CaMnO_3 (without oxygen vacancy) and $\text{CaMnO}_{2.5}$ (two oxygen vacancies per unit cell). To reveal the origin for the optimal electrical conductivity of $\text{CaMnO}_{2.75}$, DFT calculations have been carried out. As shown in Figure 9a, the calculated density of states (DOS) shows the bandgap of stoichiometric CaMnO_3 is ≈ 1.56 eV, which indicates a semiconducting behavior. As for $\text{CaMnO}_{2.75}$, the DOS profile suggests that near the Fermi level, states exist for spin-up while a gap is present for the spin-down states. This large spin polarization implies a half metallicity, which enhances the electrical conduction in metal oxides (Figure 9b). However, in the case of $\text{CaMnO}_{2.5}$, despite spin polarization, no obvious states are positioned at the Fermi level, demonstrating insignificant half-metal properties relative to $\text{CaMnO}_{2.75}$. The study proves the importance of introducing optimal concentrations of oxygen vacancies for enhancing electrical conductivity.

Moreover, the vacancy-induced electrical conductivity enhancement is also realized for HER nanocatalysts. For example, Zhang and co-workers have demonstrated an oxygen vacancy-rich metallic WO_2 -carbon mesoporous nanowires for HER.^[113] DFT calculation was performed to study the position of valence and conduction bands in addition to the projected density of states (PDOS) of the vacancy-rich WO_2 -carbon. As shown in Figure 9c,d, the simulated band structure of WO_2 -carbon shows no clear bandgap. Accordingly, the PDOS shows sharp downshift of valence and conduction bands of WO_2 -carbon. Consequently, the Fermi energy level lies in the conduction band of WO_2 -carbon, which makes it metallic and suggests enhanced electron mobility. The oxygen vacancies are also found to facilitate the charge transfer in a highly substoichiometric

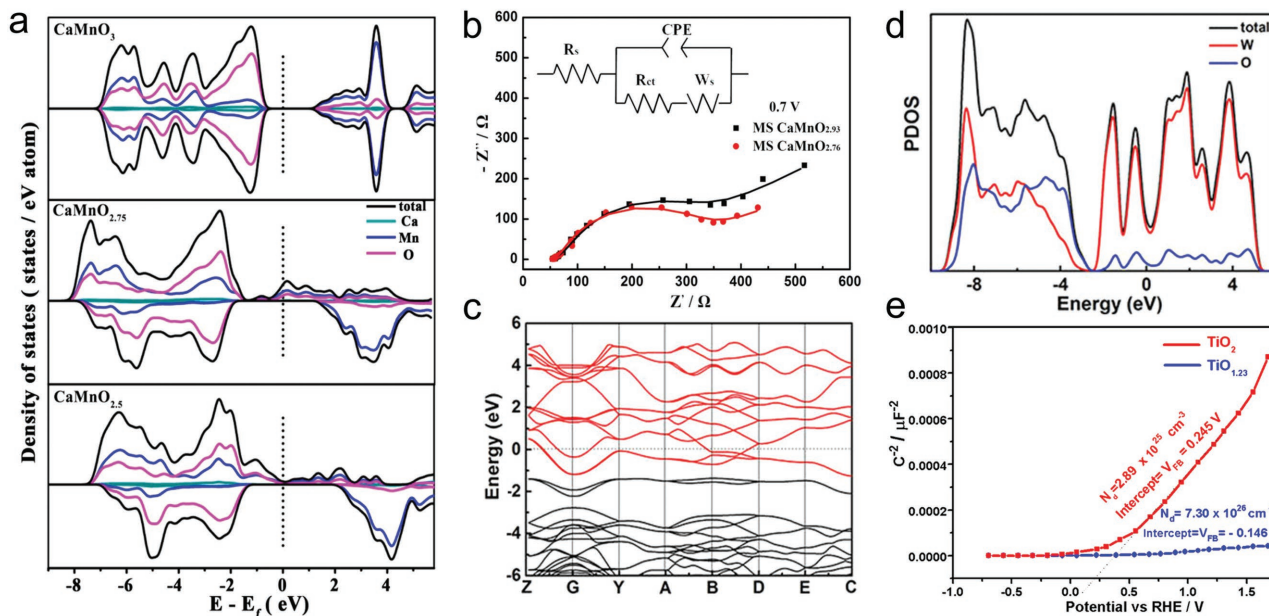


Figure 9. a) DFT calculation of the density of states (DOS) of pristine CaMnO₃, CaMnO_{2.75}, and CaMnO_{2.5}; b) electrochemical impedance spectra of pristine CaMnO_{2.93} and CaMnO_{2.76} at 0.7 V. Reproduced with permission.^[80] Copyright 2014, American Chemical Society. c) Simulated band structure and d) projected density of states of metallic WO₂-carbon mesoporous nanowires. Reproduced with permission.^[113] Copyright 2015, American Chemical Society. e) Mott-Schottky plot of TiO₂ and TiO_{1.23}. Reproduced with permission.^[82] Copyright 2016, American Chemical Society.

TiO_{1.23}. The numerous oxygen vacancies have imparted metallic behavior to TiO_{1.23}, which is confirmed by Hall effect measurement and Mott-Schottky analysis.^[82] As exemplified in Figure 9e, TiO_{1.23} exhibits a weak capacitance dependence, while a strong capacitance dependence in TiO₂ is observed, corresponding to metallic and semiconductor behaviors, respectively. In addition, the creation of vacancies renders a ≈ 25 times improvement in electron density and negative flat band potential shift of TiO_{1.23} ($7.3 \times 10^{26} \text{ cm}^{-3}$, -0.146 V) in comparison with TiO₂ ($2.89 \times 10^{25} \text{ cm}^{-3}$, 0.245 V), which infers negligible IR drop and continuous electron transport in TiO_{1.23}. This leads to an improved surface charge transfer and kinetics for HER.

In short, construction of vacancies enhances the electrical conductivity by means of narrowing the bandgaps or creating new gap states to attain a higher degree of the electron delocalization. The improvement of conductivity is responsible for the modified electron structure and accelerated charge separation and transfer process, thus leading to fast electrocatalytic reaction kinetics.

5.3. Optimization of the Kinetics Energy Barrier

Beyond tuning the density of active sites and electrical conductivity of electrocatalysts, the influence of vacancies on the kinetic energy barriers is also of great importance for water splitting. Due to the fact that the electrochemical OER and HER both involve multielementary steps from the initial to final states, it is imperative to reduce the energy barriers, i.e., activation energy (ΔG), encountered during these reaction steps. The vacancies in electrocatalysts have been widely demonstrated to effectively decrease the adsorption free energies of the OER and

HER intermediates, thus leading to a more favorable kinetic energy barrier for catalytic reactions.

For example, in the HER process, it is generally considered that the adsorption of hydrogen atom on the catalyst electrode surface forming catalyst-H*, also known as Volmer reaction, is the rate-limiting step for many HER catalysts (Figure 10a).^[47] The Gibbs free energy for the hydrogen adsorption (ΔG_{H}^*) in this step is proposed as a fundamental descriptor for HER catalytic activity. DFT has been used for calculating the free hydrogen binding energy ΔG_{H}^* and providing insights into the catalytic activity of a material. The optimal ΔG_{H}^* is calculated to be zero, which is an ideal adsorption-desorption energy of the absorbed H* to form H₂. The adsorption and desorption steps limit the overall reaction rate when the hydrogen to surface bond deviates from the optimal value. Thus, it is rational to tune the ΔG_{H}^* value of the HER catalysts close to zero and introducing vacancies into the catalysts has been proven to be an effective strategy.

In the work of Zheng and co-workers, they have shown that the creation of sulfur vacancies on the basal plane of monolayer 2H-MoS₂ can effectively change the activation energy of ΔG_{H}^* .^[74] Importantly, the optimization of ΔG_{H}^* can be facilely realized by controlling the amounts of sulfur vacancies. As shown in Figure 10b, the DFT computation indicates that the ΔG_{H}^* value of pristine 2H-MoS₂ is $\approx 2 \text{ eV}$, revealing an inert nature of the basal plane for HER. However, when a small quantity of sulfur vacancies (3.12%) is introduced, hydrogen can be stabilized on the exposed Mo atoms and the ΔG_{H}^* value significantly decreases to 0.18 eV. The ΔG_{H}^* value continues to decrease with the increase of the sulfur vacancies. For sulfur vacancies in the range of 9–19%, the ΔG_{H}^* value lies between $\pm 0.08 \text{ eV}$, which is close to the ideal value of 0 eV, denoting a low-energy barrier

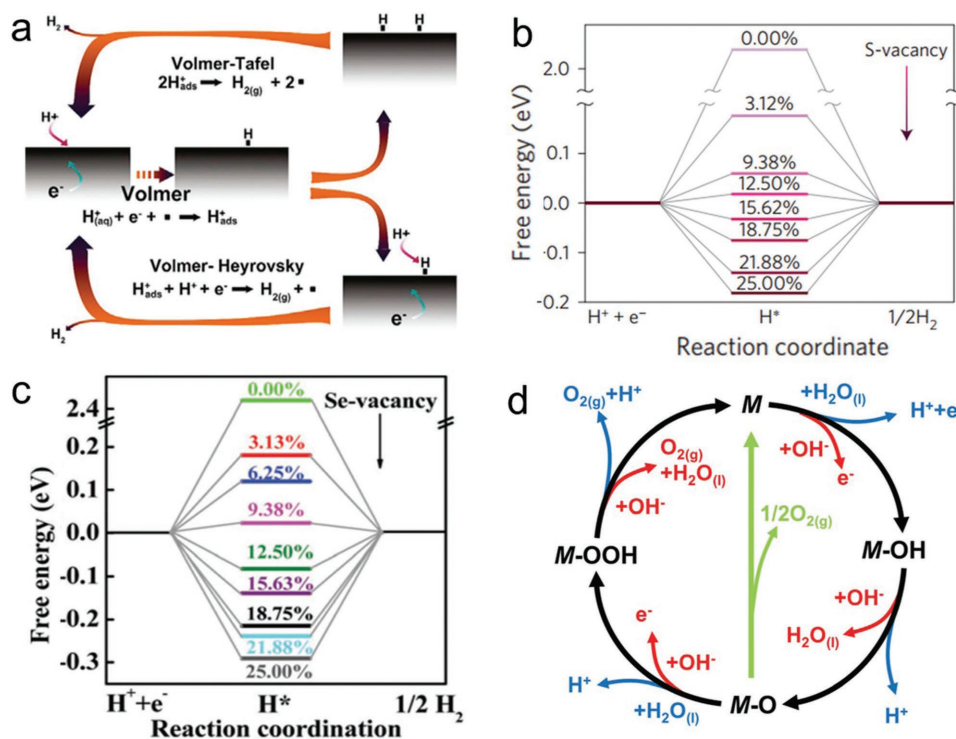


Figure 10. a) The mechanism of electrochemical HER catalysis. Reproduced with permission.^[47] Copyright 2016, Elsevier. b) Free energy versus the reaction coordinate of HER for sulfur vacancies in the range of 0–25%. Reproduced with permission.^[74] Copyright 2016, Nature Publishing Group. c) Free energy versus the reaction coordination of HER for selenium vacancies in the range of 0–25%. Reproduced with permission.^[76] Copyright 2016, Royal Society of Chemistry. d) The mechanism of electrochemical OER catalysis. Reproduced with permission.^[38] Copyright 2017, Royal Society of Chemistry.

(low overpotential) to drive the HER process. Notably, further increase of sulfur vacancies results in a negative shift of ΔG_{H^*} , which significantly strengthens the hydrogen adsorption on the catalyst, leading to detrimental HER activity. Similar variation trend toward the ΔG_{H^*} value is observed for the selenium vacancy-rich WSe_2 monolayer nanosheets.^[76] The ΔG_{H^*} value of the pristine monolayer WSe_2 basal planes is 2.44 eV. In contrast, the introduction of a suitable range of selenium vacancies decreases the ΔG_{H^*} value to 0.02–0.08 eV (Figure 10c) through the stabilization of hydrogen on the exposed W atoms, resulting in a low overpotential and high HER activity.

For OER, it typically involves four elementary reaction steps, which proceeds through the sequential formation of HO^* from adsorbed $\text{H}_2\text{O}/\text{OH}^-$, transformation to O^* and HOO^* , and finally conversion into O_2 (Figure 10d).^[38] The common consensus is that the bonding interactions between catalysts and the intermediates (OH^* , O^* , and HOO^*) are crucial for the electrocatalytic OER. The ideal thermodynamic free energy change of these intermediates should be $\Delta G_{\text{OH}^*} = \Delta G_{\text{O}^*} = \Delta G_{\text{HOO}^*} = 0$, indicating that no energy is needed to activate the reactions. The vacancy-induced effects include energy barrier reduction and intermediate oxygenated species' formation.

Qiao and co-workers have manipulated OER activity of single-crystal CoO nanorods by creating oxygen vacancies on nanofacets to optimize the adsorption energies for OER intermediates.^[85] The combined experimental and theoretical studies reveal that the vacancies are mainly located at the oxygen-terminated (111) nanofacets due to a much lower oxygen vacancy

formation energy than on the (100) and (110) facets. DFT computations are conducted to disclose the free energy diagram at 1.23 V on different facets of CoO , as shown in Figure 11a. Accordingly, the ΔG_{OOH^*} , ΔG_{O^*} , and ΔG_{OH^*} values of all intermediates in the OER process are much closer to zero with the oxygen vacancy on (111) facets, indicating a more favorable thermodynamic free energy change of the intermediates than that of the vacancy-free facets.

Such a mechanism of improved OER activity, i.e., lowering the adsorption of water molecules and intermediates by creating vacancies, has also been shown in other material systems such as perovskite oxides. Stevenson and co-workers have reported that vacancies can alter the OER pathway in an oxygen-deficient $\text{La}_{1-x}\text{Sr}_x\text{CoO}_{3-\delta}/\text{SrCoO}_{2.7}$ perovskite electrocatalyst, due to the modified electronic structures.^[86] They propose that for the vacancy-free catalyst, the OER follows a general adsorbate evolution mechanism (upper panel of Figure 11b). All intermediates during the reaction originate from the electrolyte, and Co in the active site undergoes the catalytic redox reactions. This allows Co to access a higher oxidation state of Co^{4+} . In contrast, the OER mechanism in the vacancy-rich catalyst is mediated by lattice oxygen, which allows the exchange of lattice oxygen with the adsorbed intermediate to yield the superoxide ion O_2^- rather than oxidizing Co to Co^{4+} (lower panel of Figure 11b). DFT calculations of the electrochemical OER free energy of SrCoO_3 and $\text{SrCoO}_{2.7}$ have been performed to demonstrate the switch in the reaction mechanism. The result reveals that the adsorption potential of $-\text{OH}$ to I_0 (for SrCoO_3) that complies with the

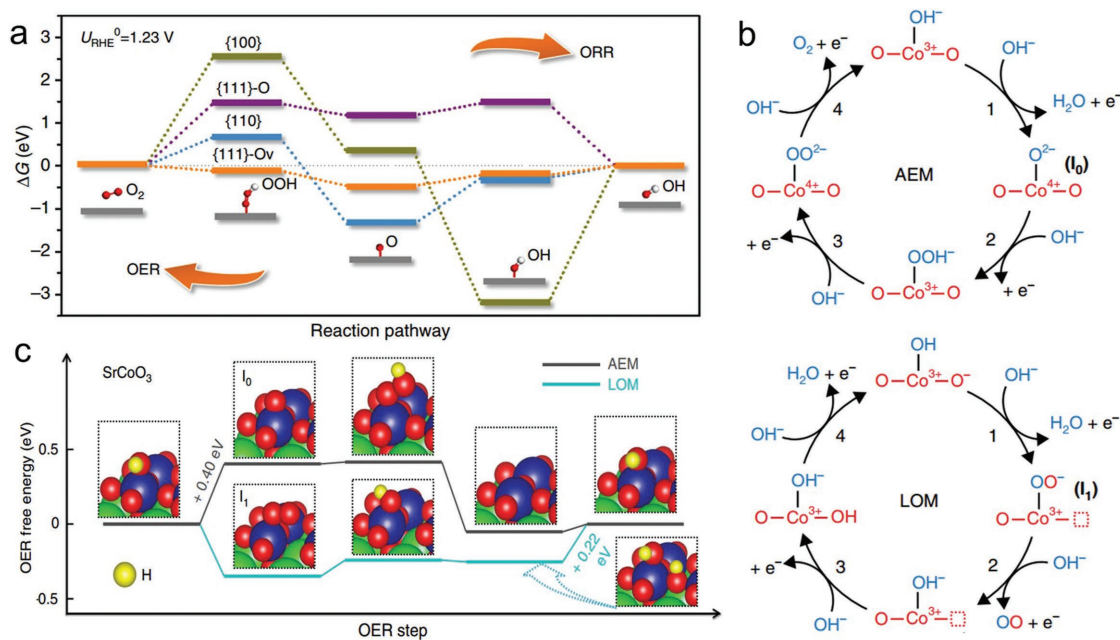


Figure 11. a) The calculated oxygen reduction reaction (ORR)/OER free energy diagram at the equilibrium potential on different CoO facets. Reproduced with permission.^[85] Copyright 2016, Nature Publishing Group. b) Oxygen evolution mechanisms on $La_{1-x}Sr_xCoO_{3-\delta}$; c) the OER free energy changes of the adsorbate evolution mechanism (AEM) and lattice oxygen-mediated mechanism (LOM) on $SrCoO_3$ at the concentration of 1/4 monolayer (ML), with indicated intermediates structures and potential-determining steps. Reproduced with permission.^[86] Copyright 2016, Nature Publishing Group.

adsorbate evolution mechanism is 0.4 V, which is the potential-determining step. However, it becomes energetically favorable when it conforms to the lattice oxygen-mediated mechanism for $SrCoO_{2.75}$. In this case, superoxide ion $-OO$ (V_O) adsorbed intermediates are formed first, which require relatively small energy barriers to evolve into $-OH$ (V_O), and electrochemically fill the vacancies by $-OH$ (aq) in the following two steps (2 and 3). The subsequent step of electrochemical deprotonation is identified as the potential-determining step, for which the computed overpotential of 0.22 V is fully consistent with experiments, as shown in Figure 11c. As such, the oxygen vacancies remarkably change the OER reaction pathway of $SrCoO_{2.75}$ and promote the proceeding of OER with a low overpotential.

In brief, introduction of vacancies alters the free energy of the intermediates or establishes new reaction pathways in the OER and HER processes. On the basis of the working mechanisms and functions of the different types of vacancies, they contribute differently to enhancing the electrochemical HER or/and OER performances. In brief, the cation vacancies mainly contribute to enhancing the OER performance of transition-metal-based nanocatalysts. This mainly originates from that the missing metal atoms which generate “positive holes” at the vacant sites, thereby beneficial for facilitating the adsorption of the H_2O molecules/ OH^- groups and promoting the transformation to other active oxyhydroxide species.^[87,88] For anion vacancies, the present review show three types of vacancies: oxygen, sulfur, and selenium vacancies. Among them, the sulfur and selenium vacancies are mostly demonstrated to introduce gap states that allow hydrogen to bind directly to the exposed metal atoms, which can tune the hydrogen adsorption free energy (ΔG) to optimal value (close to zero),^[74,76,84] and thus resulting in remarkable HER activity improvements.

On the contrary, the oxygen vacancies are generally shown to readily induce bonding between the exposed oxygen-coordination-deficient metal atoms/centers and OH^- ,^[75,85,86] which promotes the OH^- uptake and accelerates its conversion, thereby leading to enhanced OER activity. As for the multivacancies, because they are mainly composed of cation metal vacancies and oxygen vacancies,^[106–108] both of which are beneficial for the OER reactions. Consequently, the present available multivacancies in the literatures are reported to boost the OER process.

Moreover, it is noteworthy that although we discuss the functions of vacancies including tuning the density of active sites, enhancing the electrical conductivity, as well as optimizing the kinetic energy barriers separately, the underlying reason that imparts the high electrochemical OER and HER properties is due to their synergistic effects. It is undeniable that creating and engineering of vacancies at the atomic level have shown a huge effect on the reactivity of catalysts, hence constituting a strategic design toward highly efficient nanocatalyst for water splitting.

6. Conclusion and Future Perspectives

In this review, we have given an overview of the recent literatures in exploring and studying of vacancy-rich noble-metal-free nanocatalysts for efficient electrochemical water splitting. Engineering favorable vacancies on the electrocatalysts has demonstrated to boost the sluggish reaction thermodynamics and kinetics. The great progresses achieved by different research groups in this field provide a new fertile ground for the development of high-performance nonprecious electrocatalysts toward efficient energy conversion. In spite of the significant

achievements described in this review, some challenges as well as opportunities remain in this relatively nascent field. Further attention can be devoted to the following aspects.

First, the existing vacancy-rich nanocatalysts are mostly rich of anion vacancies, especially of oxygen vacancies. The fabrication and application of other types of vacancies (i.e., metal-cation-deficient materials) are still limited. Given the diverse composition of the nonprecious transition-metal-based electrocatalysts, novel anion (such as P, N, and C), cation, as well as multivacancies can be exploited. This will enrich the varieties of vacancy-rich nanocatalysts and lead to the further advancement of electrochemical water splitting.

Second, the recent advances made on exploring novel vacancy-rich electrocatalysts highlight that the vacancy engineering not only tunes the activity of commonly active catalysts, but also endows the pristine electroinactive materials with high performance. This has been demonstrated by two paradigms of oxygen vacancy-rich metallic titania ($\text{TiO}_{1.23}$)^[82] and concave Bi_2WO_6 nanoplates^[81] recently. The tailoring of vacancies presents unique feature for designing and fabricating novel nonprecious electrocatalysts for water splitting, which is difficult to be realized by the traditional morphology and size tuning approaches.

Third, at present, although most of reported studies of vacancy-rich nanomaterials highlight that the vacancies are beneficial for electrocatalytic applications, there are still some conflict reports.^[129,132] For example, Smith and co-workers studied oxygen vacancies in perovskite SrCoO_3 using first principles calculations from thermodynamic, electronic, and kinetic points of view. They investigated the effect of surface vacancies on the OER activity and found that oxygen vacancies are detrimental to the performance.^[132] In this context, in-depth fundamental investigations of the vacancy-induced catalytic activity, especially with the modern in situ or operando spectroscopic and microscopic characterizations, are desirable. This would provide scientific guidance regarding how to optimize the catalyst performance through the engineering of vacancies.

Finally, considering the outstanding performances of the vacancy-rich nanocatalysts that have been realized, further improvement of the catalytic activity can be expected when other strategies such as doping, straining, or hybridizing with conducting substrates (e.g., metal or carbon materials) are combined with the vacancy-modification method. Through the collective, harmonious optimization of the components, material structure, as well as interfacial interaction, the exploration of highly efficient nonprecious nanocatalysts for practical application of electrochemical water splitting is anticipated.

Acknowledgements

This research is supported by the National Research Foundation (NRF) under the Energy Innovation Research Programme (EIRP) R-263-000-B82-279, managed on behalf of The Building and Construction Authority (BCA).

Conflict of Interest

The authors declare no conflict of interest.

Keywords

electrocatalytic water splitting, noble metal-free nanocatalysts, transition-metal-based materials, vacancies

Received: September 25, 2017

Revised: October 31, 2017

Published online: January 22, 2018

- [1] M.-Q. Yang, Y.-J. Xu, W. Lu, K. Zeng, H. Zhu, Q.-H. Xu, G. W. Ho, *Nat. Commun.* **2017**, *8*, 14224.
- [2] M.-Q. Yang, J. Dan, S. J. Pennycook, X. Lu, H. Zhu, Q.-H. Xu, H. J. Fan, G. W. Ho, *Mater. Horiz.* **2017**, *4*, 885.
- [3] L. Zhu, C. Fu Tan, M. Gao, G. W. Ho, *Adv. Mater.* **2015**, *27*, 7713.
- [4] C. F. Tan, W. L. Ong, G. W. Ho, *ACS Nano* **2015**, *9*, 7661.
- [5] M. Gao, P. K. N. Connor, G. W. Ho, *Energy Environ. Sci.* **2016**, *9*, 3151.
- [6] M.-Q. Yang, N. Zhang, Y. Wang, Y.-J. Xu, *J. Catal.* **2017**, *346*, 21.
- [7] M.-Q. Yang, Y.-J. Xu, *Nanoscale Horiz.* **2016**, *1*, 185.
- [8] L. Zhu, M. Hong, G. W. Ho, *Nano Energy* **2015**, *11*, 28.
- [9] M. Gao, L. Zhu, W. L. Ong, J. Wang, G. W. Ho, *Catal. Sci. Technol.* **2015**, *5*, 4703.
- [10] N. Zhang, C. Han, Y.-J. Xu, J. J. Foley IV, D. Zhang, J. Codrington, S. K. Gray, Y. Sun, *Nat. Photonics* **2016**, *10*, 473.
- [11] N. Zhang, M.-Q. Yang, S. Liu, Y. Sun, Y.-J. Xu, *Chem. Rev.* **2015**, *115*, 10307.
- [12] M.-Q. Yang, N. Zhang, M. Pagliaro, Y.-J. Xu, *Chem. Soc. Rev.* **2014**, *43*, 8240.
- [13] K. Xu, J. Wu, C. F. Tan, G. W. Ho, A. Wei, M. Hong, *Nanoscale* **2017**, *9*, 11574.
- [14] G. Yilmaz, K. M. Yam, C. Zhang, H. J. Fan, G. W. Ho, *Adv. Mater.* **2017**, *29*, 1606814.
- [15] J. Wang, C. F. Tan, T. Zhu, G. W. Ho, *Angew. Chem., Int. Ed.* **2016**, *55*, 10326.
- [16] W. Y. Lim, Y. F. Lim, G. W. Ho, *J. Mater. Chem. A* **2017**, *5*, 919.
- [17] T. Zhu, L. Zhu, J. Wang, G. W. Ho, *J. Mater. Chem. A* **2016**, *4*, 13916.
- [18] T. Zhu, L. Zhu, J. Wang, G. W. Ho, *ACS Appl. Mater. Interfaces* **2016**, *8*, 32901.
- [19] Y. Zhang, X. Xia, X. Cao, B. Zhang, N. H. Tiep, H. He, S. Chen, Y. Huang, H. J. Fan, *Adv. Energy Mater.* **2017**, *7*, 1700220.
- [20] X. Cui, P. Xiao, J. Wang, M. Zhou, W. Guo, Y. Yang, Y. He, Z. Wang, Y. Yang, Y. Zhang, Z. Lin, *Angew. Chem., Int. Ed.* **2017**, *56*, 4488.
- [21] H. Liang, A. N. Gandi, C. Xia, M. N. Hedhili, D. H. Anjum, U. Schwingenschlöggl, H. N. Alshareef, *ACS Energy Lett.* **2017**, *2*, 1035.
- [22] H. Liang, A. N. Gandi, D. H. Anjum, X. Wang, U. Schwingenschlöggl, H. N. Alshareef, *Nano Lett.* **2016**, *16*, 7718.
- [23] T. Zhu, J. Wang, G. W. Ho, *Nano Energy* **2015**, *18*, 273.
- [24] S. W. L. Ng, G. Yilmaz, W. L. Ong, G. W. Ho, *Appl. Catal., B* **2018**, *220*, 533.
- [25] L. Zhu, C. K. Nuo Peh, T. Zhu, Y.-F. Lim, G. W. Ho, *J. Mater. Chem. A* **2017**, *5*, 8343.
- [26] X. Xia, J. Zhan, Y. Zhong, X. Wang, J. Tu, H. J. Fan, *Small* **2017**, *13*, 1602742.
- [27] C. Zhu, L. Yang, J. K. Seo, X. Zhang, S. Wang, J. Shin, D. Chao, H. Zhang, Y. S. Meng, H. J. Fan, *Mater. Horiz.* **2017**, *4*, 415.
- [28] C. Xia, Q. Jiang, C. Zhao, P. M. Beaujuge, H. N. Alshareef, *Nano Energy* **2016**, *24*, 78.
- [29] H. Hu, Z. Pei, H. Fan, C. Ye, *Small* **2016**, *12*, 3059.
- [30] Y. Li, H. Dai, *Chem. Soc. Rev.* **2014**, *43*, 5257.
- [31] T. Zhang, Z. Tao, J. Chen, *Mater. Horiz.* **2014**, *1*, 196.

- [32] X. Xia, D. Chao, Y. Zhang, J. Zhan, Y. Zhong, X. Wang, Y. Wang, Z. X. Shen, J. Tu, H. J. Fan, *Small* **2016**, *12*, 3048.
- [33] B. Jiang, Y. He, B. Li, S. Zhao, S. Wang, Y.-B. He, Z. Lin, *Angew. Chem., Int. Ed.* **2017**, *56*, 1869.
- [34] S. Wu, C. Han, J. Iocozzia, M. Lu, R. Ge, R. Xu, Z. Lin, *Angew. Chem., Int. Ed.* **2016**, *55*, 7898.
- [35] F. Zhang, C. Xia, J. Zhu, B. Ahmed, H. Liang, D. B. Velusamy, U. Schwingenschlögl, H. N. Alshareef, *Adv. Energy Mater.* **2016**, *6*, 1601188.
- [36] C. Wang, S. Wang, L. Tang, Y.-B. He, L. Gan, J. Li, H. Du, B. Li, Z. Lin, F. Kang, *Nano Energy* **2016**, *21*, 133.
- [37] F. Zhang, J. Zhu, D. Zhang, U. Schwingenschlögl, H. N. Alshareef, *Nano Lett.* **2017**, *17*, 1302.
- [38] N.-T. Suen, S.-F. Hung, Q. Quan, N. Zhang, Y.-J. Xu, H. M. Chen, *Chem. Soc. Rev.* **2017**, *46*, 337.
- [39] S. Anantharaj, S. R. Ede, K. Sakthikumar, K. Karthick, S. Mishra, S. Kundu, *ACS Catal.* **2016**, *6*, 8069.
- [40] P. Xiao, W. Chen, X. Wang, *Adv. Energy Mater.* **2015**, *5*, 1500985.
- [41] J. Li, G. Zheng, *Adv. Sci.* **2017**, *4*, 1600380.
- [42] S. Y. Tee, K. Y. Win, W. S. Teo, L.-D. Koh, S. Liu, C. P. Teng, M.-Y. Han, *Adv. Sci.* **2017**, *4*, 1600337.
- [43] W. T. Hong, M. Risch, K. A. Stoerzinger, A. Grimaud, J. Suntivich, Y. Shao-Horn, *Energy Environ. Sci.* **2015**, *8*, 1404.
- [44] I. Roger, M. A. Shipman, M. D. Symes, *Nat. Rev. Chem.* **2017**, *1*, 0003.
- [45] D. Yan, Y. Li, J. Huo, R. Chen, L. Dai, S. Wang, *Adv. Mater.* **2017**, *29*, 1606459.
- [46] J. Luo, J.-H. Im, M. T. Mayer, M. Schreier, M. K. Nazeeruddin, N.-G. Park, S. D. Tilley, H. J. Fan, M. Grätzel, *Science* **2014**, *345*, 1593.
- [47] Q. Ding, B. Song, P. Xu, S. Jin, *Chem* **2016**, *1*, 699.
- [48] L. Han, S. Dong, E. Wang, *Adv. Mater.* **2016**, *28*, 9266.
- [49] W. Zhang, K. Zhou, *Small* **2017**, *13*, 1700806.
- [50] J. Wang, W. Cui, Q. Liu, Z. Xing, A. M. Asiri, X. Sun, *Adv. Mater.* **2016**, *28*, 215.
- [51] Y. Xu, B. Zhang, *Chem. Soc. Rev.* **2014**, *43*, 2439.
- [52] Y. Lee, J. Suntivich, K. J. May, E. E. Perry, Y. Shao-Horn, *J. Phys. Chem. Lett.* **2012**, *3*, 399.
- [53] Y.-Y. Chen, Y. Zhang, W.-J. Jiang, X. Zhang, Z. Dai, L.-J. Wan, J.-S. Hu, *ACS Nano* **2016**, *10*, 8851.
- [54] R. Chen, C. Yang, W. Cai, H.-Y. Wang, J. Miao, L. Zhang, S. Chen, B. Liu, *ACS Energy Lett.* **2017**, *2*, 1070.
- [55] S. Cherevko, S. Geiger, O. Kasian, N. Kulyk, J.-P. Grote, A. Savan, B. R. Shrestha, S. Merzlikin, B. Breitbach, A. Ludwig, K. J. J. Mayrhofer, *Catal. Today* **2016**, *262*, 170.
- [56] H. Liang, H. N. Alshareef, *Small Methods* **2017**, *1*, 1700111.
- [57] M. Gong, D.-Y. Wang, C.-C. Chen, B.-J. Hwang, H. Dai, *Nano Res.* **2016**, *9*, 28.
- [58] X. Long, Z. Wang, S. Xiao, Y. An, S. Yang, *Mater. Today* **2016**, *19*, 213.
- [59] M. S. Burke, L. J. Enman, A. S. Batchellor, S. Zou, S. W. Boettcher, *Chem. Mater.* **2015**, *27*, 7549.
- [60] Y. Wang, B. Kong, D. Zhao, H. Wang, C. Selomulya, *Nano Today* **2017**, *15*, 26.
- [61] H. Zhao, Z.-Y. Yuan, *Catal. Sci. Technol.* **2017**, *7*, 330.
- [62] B. You, N. Jiang, M. Sheng, M. W. Bhushan, Y. Sun, *ACS Catal.* **2016**, *6*, 714.
- [63] B. You, N. Jiang, X. Liu, Y. Sun, *Angew. Chem., Int. Ed.* **2016**, *55*, 9913.
- [64] B. You, N. Jiang, M. Sheng, S. Gul, J. Yano, Y. Sun, *Chem. Mater.* **2015**, *27*, 7636.
- [65] B. You, X. Liu, N. Jiang, Y. Sun, *J. Am. Chem. Soc.* **2016**, *138*, 13639.
- [66] G. Li, G. R. Blake, T. T. M. Palstra, *Chem. Soc. Rev.* **2017**, *46*, 1693.
- [67] J. Jia, C. Qian, Y. Dong, Y. F. Li, H. Wang, M. Ghossoub, K. T. Butler, A. Walsh, G. A. Ozin, *Chem. Soc. Rev.* **2017**, *46*, 4631.
- [68] Y. Sun, S. Gao, F. Lei, C. Xiao, Y. Xie, *Acc. Chem. Res.* **2015**, *48*, 3.
- [69] Y. Sun, S. Gao, F. Lei, Y. Xie, *Chem. Soc. Rev.* **2015**, *44*, 623.
- [70] X. Pan, M.-Q. Yang, X. Fu, N. Zhang, Y.-J. Xu, *Nanoscale* **2013**, *5*, 3601.
- [71] C. T. Campbell, C. H. F. Peden, *Science* **2005**, *309*, 713.
- [72] J. F. Weaver, F. Zhang, L. Pan, T. Li, A. Asthagiri, *Acc. Chem. Res.* **2015**, *48*, 1515.
- [73] C. Tsai, H. Li, S. Park, J. Park, H. S. Han, J. K. Nørskov, X. Zheng, F. Abild-Pedersen, *Nat. Commun.* **2017**, *8*, 15113.
- [74] H. Li, C. Tsai, A. L. Koh, L. Cai, A. W. Contryman, A. H. Fragapane, J. Zhao, H. S. Han, H. C. Manoharan, F. Abild-Pedersen, J. K. Nørskov, X. Zheng, *Nat. Mater.* **2016**, *15*, 48.
- [75] J. Kim, X. Yin, K.-C. Tsao, S. Fang, H. Yang, *J. Am. Chem. Soc.* **2014**, *136*, 14646.
- [76] Y. Sun, X. Zhang, B. Mao, M. Cao, *Chem. Commun.* **2016**, *52*, 14266.
- [77] X. Zhou, J. Jiang, T. Ding, J. Zhang, B. Pan, J. Zuo, Q. Yang, *Nanoscale* **2014**, *6*, 11046.
- [78] L. Xu, Q. Jiang, Z. Xiao, X. Li, J. Huo, S. Wang, L. Dai, *Angew. Chem., Int. Ed.* **2016**, *55*, 5277.
- [79] Y. Zhao, C. Chang, F. Teng, Y. Zhao, G. Chen, R. Shi, G. I. N. Waterhouse, W. Huang, T. Zhang, *Adv. Energy Mater.* **2017**, *7*, 1700005.
- [80] J. Du, T. Zhang, F. Cheng, W. Chu, Z. Wu, J. Chen, *Inorg. Chem.* **2014**, *53*, 9106.
- [81] Z.-P. Nie, D.-K. Ma, G.-Y. Fang, W. Chen, S.-M. Huang, *J. Mater. Chem. A* **2016**, *4*, 2438.
- [82] J. Swaminathan, R. Subbiah, V. Singaram, *ACS Catal.* **2016**, *6*, 2222.
- [83] Y. Wang, T. Zhou, K. Jiang, P. Da, Z. Peng, J. Tang, B. Kong, W.-B. Cai, Z. Yang, G. Zheng, *Adv. Energy Mater.* **2014**, *4*, 1400696.
- [84] A.-Y. Lu, X. Yang, C.-C. Tseng, S. Min, S.-H. Lin, C.-L. Hsu, H. Li, H. Idriss, J.-L. Kuo, K.-W. Huang, L.-J. Li, *Small* **2016**, *12*, 5530.
- [85] T. Ling, D.-Y. Yan, Y. Jiao, H. Wang, Y. Zheng, X. Zheng, J. Mao, X.-W. Du, Z. Hu, M. Jaroniec, S.-Z. Qiao, *Nat. Commun.* **2016**, *7*, 12876.
- [86] J. T. Mefford, X. Rong, A. M. Abakumov, W. G. Hardin, S. Dai, A. M. Kolpak, K. P. Johnston, K. J. Stevenson, *Nat. Commun.* **2016**, *7*, 11053.
- [87] J. Zhu, Z. Ren, S. Du, Y. Xie, J. Wu, H. Meng, Y. Xue, H. Fu, *Nano Res.* **2017**, *10*, 1819.
- [88] Y. Liu, H. Cheng, M. Lyu, S. Fan, Q. Liu, W. Zhang, Y. Zhi, C. Wang, C. Xiao, S. Wei, B. Ye, Y. Xie, *J. Am. Chem. Soc.* **2014**, *136*, 15670.
- [89] Y. Zhou, C.-K. Dong, L. L. Han, J. Yang, X.-W. Du, *ACS Catal.* **2016**, *6*, 6699.
- [90] G. Zhang, J. Yang, H. Wang, H. Chen, J. Yang, F. Pan, *ACS Appl. Mater. Interfaces* **2017**, *9*, 16159.
- [91] J. Wang, L. Li, H. Tian, Y. Zhang, X. Che, G. Li, *ACS Appl. Mater. Interfaces* **2017**, *9*, 7100.
- [92] L. Zhuang, L. Ge, Y. Yang, M. Li, Y. Jia, X. Yao, Z. Zhu, *Adv. Mater.* **2017**, *29*, 1606793.
- [93] Y. Chen, J. Hu, H. Diao, W. Luo, Y.-F. Song, *Chem.–Eur. J.* **2017**, *23*, 4010.
- [94] X. Lei, W. Zhimin, W. Jialu, X. Zhaohui, H. Xiaobing, L. Zhigang, W. Shuangyin, *Nanotechnology* **2017**, *28*, 165402.
- [95] C. Hu, L. Zhang, Z.-J. Zhao, J. Luo, J. Shi, Z. Huang, J. Gong, *Adv. Mater.* **2017**, *29*, 1701820.
- [96] Y.-Z. Su, Q.-Z. Xu, G.-F. Chen, H. Cheng, N. Li, Z.-Q. Liu, *Electrochim. Acta* **2015**, *174*, 1216.
- [97] C. Zhu, S. Fu, D. Du, Y. Lin, *Chem.–Eur. J.* **2016**, *22*, 4000.
- [98] J. Bao, X. Zhang, B. Fan, J. Zhang, M. Zhou, W. Yang, X. Hu, H. Wang, B. Pan, Y. Xie, *Angew. Chem., Int. Ed.* **2015**, *54*, 7399.

- [99] Z. Wang, Y. You, J. Yuan, Y.-X. Yin, Y.-T. Li, S. Xin, D. Zhang, *ACS Appl. Mater. Interfaces* **2016**, *8*, 6520.
- [100] D. Chen, J. Wang, Z. Zhang, Z. Shao, F. Ciucci, *Chem. Commun.* **2016**, *52*, 10739.
- [101] Y. Yin, J. Han, Y. Zhang, X. Zhang, P. Xu, Q. Yuan, L. Samad, X. Wang, Y. Wang, Z. Zhang, P. Zhang, X. Cao, B. Song, S. Jin, *J. Am. Chem. Soc.* **2016**, *138*, 7965.
- [102] X. Chen, Z. Wang, Y. Qiu, J. Zhang, G. Liu, W. Zheng, W. Feng, W. Cao, P. Hu, W. Hu, *J. Mater. Chem. A* **2016**, *4*, 18060.
- [103] Y. Xu, L. Wang, X. Liu, S. Zhang, C. Liu, D. Yan, Y. Zeng, Y. Pei, Y. Liu, S. Luo, *J. Mater. Chem. A* **2016**, *4*, 16524.
- [104] C.-C. Cheng, A.-Y. Lu, C.-C. Tseng, X. Yang, M. N. Hedhili, M.-C. Chen, K.-H. Wei, L.-J. Li, *Nano Energy* **2016**, *30*, 846.
- [105] G. Wu, W. Chen, X. Zheng, D. He, Y. Luo, X. Wang, J. Yang, Y. Wu, W. Yan, Z. Zhuang, X. Hong, Y. Li, *Nano Energy* **2017**, *38*, 167.
- [106] Y. Zhu, W. Zhou, J. Yu, Y. Chen, M. Liu, Z. Shao, *Chem. Mater.* **2016**, *28*, 1691.
- [107] Y. Wang, Y. Zhang, Z. Liu, C. Xie, S. Feng, D. Liu, M. Shao, S. Wang, *Angew. Chem., Int. Ed.* **2017**, *56*, 5867.
- [108] R. Liu, Y. Wang, D. Liu, Y. Zou, S. Wang, *Adv. Mater.* **2017**, *29*, 1701546.
- [109] V. Nicolosi, M. Chhowalla, M. G. Kanatzidis, M. S. Strano, J. N. Coleman, *Science* **2013**, *340*, 1226419.
- [110] Y. Maimaiti, M. Nolan, S. D. Elliott, *Phys. Chem. Chem. Phys.* **2014**, *16*, 3036.
- [111] T. Pussacq, H. Kabbour, S. Colis, H. Vezin, S. Saitzek, O. Gardoll, C. Tassel, H. Kageyama, C. Laberty Robert, O. Mentré, *Chem. Mater.* **2017**, *29*, 1047.
- [112] J. Lu, A. Carvalho, X. K. Chan, H. Liu, B. Liu, E. S. Tok, K. P. Loh, A. H. Castro Neto, C. H. Sow, *Nano Lett.* **2015**, *15*, 3524.
- [113] R. Wu, J. Zhang, Y. Shi, D. Liu, B. Zhang, *J. Am. Chem. Soc.* **2015**, *137*, 6983.
- [114] F. Cheng, T. Zhang, Y. Zhang, J. Du, X. Han, J. Chen, *Angew. Chem., Int. Ed.* **2013**, *52*, 2474.
- [115] Y. Guo, Y. Tong, P. Chen, K. Xu, J. Zhao, Y. Lin, W. Chu, Z. Peng, C. Wu, Y. Xie, *Adv. Mater.* **2015**, *27*, 5989.
- [116] E. Korin, N. Froumin, S. Cohen, *ACS Biomater. Sci. Eng.* **2017**, *3*, 882.
- [117] C. Corbel, M. Stucky, P. Hautojärvi, K. Saarinen, P. Moser, *Phys. Rev. B* **1988**, *38*, 8192.
- [118] P. Asoka-Kumar, M. Alatalo, V. J. Ghosh, A. C. Kruseman, B. Nielsen, K. G. Lynn, *Phys. Rev. Lett.* **1996**, *77*, 2097.
- [119] M. Alatalo, B. Barbiellini, M. Hakala, H. Kauppinen, T. Korhonen, M. J. Puska, K. Saarinen, P. Hautojärvi, R. M. Nieminen, *Phys. Rev. B* **1996**, *54*, 2397.
- [120] K. Saarinen, P. Hautojärvi, C. Corbel, in *Semiconductors and Semimetals*, Vol. 51 (Ed.: M. Stavola), Elsevier, New York, NY **1998**, Ch. 5, p. 209.
- [121] X. Liu, K. Zhou, L. Wang, B. Wang, Y. Li, *J. Am. Chem. Soc.* **2009**, *131*, 3140.
- [122] R.-A. Eichel, *Phys. Chem. Chem. Phys.* **2011**, *13*, 368.
- [123] R. Stoyanova, E. Zhecheva, C. Friebel, *Solid State Ionics* **1994**, *73*, 1.
- [124] P. Lommens, F. Loncke, P. F. Smet, F. Callens, D. Poelman, H. Vrielinck, Z. Hens, *Chem. Mater.* **2007**, *19*, 5576.
- [125] S. Mandal, R. M. Rojas, J. M. Amarilla, P. Calle, N. V. Kosova, V. F. Anufrienko, J. M. Rojo, *Chem. Mater.* **2002**, *14*, 1598.
- [126] J. M. Gaite, P. Ermakoff, J. P. Muller, *Phys. Chem. Miner.* **1993**, *20*, 242.
- [127] B. D. Shrivastava, *J. Phys.: Conf. Ser.* **2012**, *365*, 012002.
- [128] Y. Zhao, X. Jia, G. Chen, L. Shang, G. I. N. Waterhouse, L.-Z. Wu, C.-H. Tung, D. O'Hare, T. Zhang, *J. Am. Chem. Soc.* **2016**, *138*, 6517.
- [129] J. Zhang, W. Xiao, P. Xi, S. Xi, Y. Du, D. Gao, J. Ding, *ACS Energy Lett.* **2017**, *2*, 1022.
- [130] D. Voiry, R. Fullon, J. Yang, C. de Carvalho Castro e Silva, R. Kappera, I. Bozkurt, D. Kaplan, M. J. Lajos, P. E. Batson, G. Gupta, A. D. Mohite, L. Dong, D. Er, V. B. Shenoy, T. Asefa, M. Chhowalla, *Nat. Mater.* **2016**, *15*, 1003.
- [131] H. Li, M. Du, M. J. Mleczko, A. L. Koh, Y. Nishi, E. Pop, A. J. Bard, X. Zheng, *J. Am. Chem. Soc.* **2016**, *138*, 5123.
- [132] H. A. Tahini, X. Tan, U. Schwingenschlögl, S. C. Smith, *ACS Catal.* **2016**, *6*, 5565.
- [133] L. Li, T. Tian, J. Jiang, L. Ai, *J. Power Sources* **2015**, *294*, 103.
- [134] I. Abidat, N. Bouchenafa-Saib, A. Habrioux, C. Comminges, C. Canaff, J. Rousseau, T. W. Napporn, D. Dambournet, O. Borkiewicz, K. B. Kokoh, *J. Mater. Chem. A* **2015**, *3*, 17433.
- [135] W. Song, Z. Ren, S.-Y. Chen, Y. Meng, S. Biswas, P. Nandi, H. A. Elsen, P.-X. Gao, S. L. Suib, *ACS Appl. Mater. Interfaces* **2016**, *8*, 20802.
- [136] Y.-R. Liu, G.-Q. Han, X. Li, B. Dong, X. Shang, W.-H. Hu, Y.-M. Chai, Y.-Q. Liu, C.-G. Liu, *Int. J. Hydrogen Energy* **2016**, *41*, 12976.
- [137] X. Zhao, Y. Fu, J. Wang, Y. Xu, J.-H. Tian, R. Yang, *Electrochim. Acta* **2016**, *201*, 172.
- [138] J.-J. Zhang, H.-H. Wang, T.-J. Zhao, K.-X. Zhang, X. Wei, Z.-D. Jiang, S.-I. Hirano, X.-H. Li, J.-S. Chen, *ChemSusChem* **2017**, *10*, 2875.
- [139] C.-F. Chen, G. King, R. M. Dickerson, P. A. Papin, S. Gupta, W. R. Kellogg, G. Wu, *Nano Energy* **2015**, *13*, 423.
- [140] F. Song, K. Schenk, X. Hu, *Energy Environ. Sci.* **2016**, *9*, 473.
- [141] Z. Luo, R. Miao, T. D. Huan, I. M. Mosa, A. S. Poyraz, W. Zhong, J. E. Cloud, D. A. Kriz, S. Thanneeru, J. He, Y. Zhang, R. Ramprasad, S. L. Suib, *Adv. Energy Mater.* **2016**, *6*, 1600528.
- [142] X. Xie, W. Mu, X. Li, H. Wei, Y. Jian, Q. Yu, R. Zhang, K. Lv, H. Tang, S. Luo, *Electrochim. Acta* **2014**, *134*, 201.
- [143] L. Li, T. Zhang, J. Yan, X. Cai, S. Liu, *Small* **2017**, *13*, 1700441.
- [144] J. Yu, W. Zhou, T. Xiong, A. Wang, S. Chen, B. Chu, *Nano Res.* **2017**, *10*, 2599.